Geosci. Model Dev. Discuss., 6, 4345–4416, 2013
www.geosci-model-dev-discuss.net/6/4345/2013/
doi:10.5194/gmdd-6-4345-2013

Geoscientific Model Development Discussions
Open Access

Aircraft routing with minimal climate impact: the REACT4C climate cost function modelling approach (V1.0)

V. Grewe[1], C. Frömming[1], S. Matthes[1], S. Brinkop[1], M. Ponater[1], S. Dietmüller[1], P. Jöckel[1], H. Garny[1], E. Tsati[1], O. A. Søvde[2], J. Fuglestvedt[2], T. K. Berntsen[2], K. P. Shine[3], E. A. Irvine[3], T. Champougny[4], and P. Hullah[5]

[1]Deutsches Zentrum für Luft- und Raumfahrt, Institut für Physik der Atmosphäre, Oberpfaffenhofen, Germany
[2]Center for International Climate and Environmental Research Oslo (CICERO), Oslo, Norway
[3]Department of Meteorology, University of Reading, Reading, UK
[4]Eurocontrol Headquarter DNM/OPL, Brussels, Belgium
[5]Eurocontrol Experimental Centre, Bretigny, France

Received: 1 August 2013 – Accepted: 5 August 2013 – Published: 12 August 2013

Correspondence to: V. Grewe (volker.grewe@dlr.de)

Published by Copernicus Publications on behalf of the European Geosciences Union.

Abstract

In addition to CO_2, the climate impact of aviation is strongly influenced by non-CO_2 emissions, such as nitrogen oxides, influencing ozone and methane, and water vapour, forming contrails. Because these non-CO_2 emission effects are characterised by a short lifetime, their climate impact largely depends on emission location and time, i.e. emissions in certain locations (or times) can lead to a greater climate impact (even on the global average) than the same emission in other locations (or times). Avoiding these climate sensitive regions might thus be beneficial to climate. Here, we describe a modelling chain for investigating this climate impact mitigation option. It forms a multi-step modelling approach, starting with the simulation of the fate of emissions released at a certain location and time (time-region). This is performed with the chemistry–climate model EMAC, extended by the two submodels AIRTRAC 1.0 and CONTRAIL 1.0, which describe the contribution of emissions to the composition of the atmosphere and the contrail formation. Numerous time-regions are efficiently calculated by applying a Lagrangian scheme. EMAC also includes the calculation of radiative impacts, which are, in a second step, the input to climate metric formulas describing the climate impact of the time-region emission. The result of the modelling chain comprises a four dimensional dataset in space and time, which we call *climate cost functions*, and which describe at each grid point and each point in time, the climate impact of an emission. In a third step, these climate cost functions are used in a traffic simulator (SAAM), coupled to an emission tool (AEM) to optimise aircraft trajectories for the North Atlantic region. Here, we describe the details of this new modelling approach and show some example results. A number of sensitivity analyses are performed to motivate the settings of individual parameters. A stepwise sanity check of the results of the modelling chain is undertaken to demonstrate the plausibility of the climate cost functions.

GMDD
6, 4345–4416, 2013

1 Introduction

The anthropogenic origin of a substantial contribution of observed climate change is well established (e.g., IPCC, 2007). The challenge is how to deal with climate change and to find and evaluate mitigation strategies. Air traffic has a significant contribution to total anthropogenic climate change (Berntsen and Fuglestvedt, 2008; Lee et al., 2010; Burkhardt and Kärcher, 2011) and a significant part of its contribution is arising from non-CO_2 emissions, e.g. from changes in ozone, methane, cloudiness, and others.

These non-CO_2 effects are characterised by a high temporal and spatial variability, i.e. their impact on climate depends not only on the amount of emitted species, as in the case of CO_2, but also on the time and region where the emissions take place. The formation and persistence of contrails depend on both, aircraft and fuel parameters, and meteorological conditions (Schumann, 1996), such as ice supersaturation. These ice supersaturated regions are locally and temporarily very confined and show a large variability (Spichtinger et al., 2003; Gierens and Spichtinger, 2000) and a dependence on the prevailing weather condition (Irvine et al., 2012). Contrails may persist for a long time under favourable weather conditions (Minnis et al., 1998; Burkhardt and Kärcher, 2009). The variability of the climate impact from NO_x emissions with respect to weather conditions has not been investigated yet. Climatological studies (Grewe and Stenke, 2008; Köhler et al., 2008; Frömming et al., 2012) show a distinct altitude and latitude variability. For an individual weather situation this variability is probably enlarged, since an emission taking place in a region with cloud formation and rain will have a significantly lower impact than an emission taking place in a region with upwelling, increasing the lifetime of the emitted species.

Within the EU-project REACT4C, we quantify this variability and use it to develop possible strategies whereby aircraft are routed to minimise their total climate impact. It is likely that the fuel consumption increases for these aircraft trajectories, because in general (although not always) aircraft take routes that are close to the minimum fuel (and hence mininum CO_2 emission) route. In this case the gain from non-CO_2

GMDD
6, 4345–4416, 2013

effects counteracts the CO_2 induced warming, at least to some extent. How strong this compensation effect is, also depends on the objective. It will be stronger if the objective is on long-term climate change, since then CO_2 effects are more pronounced. Thereby it depends on the chosen time frame (or time horizon) and the adopted indicator of climate change.

Basically this optimisation is based on two major steps, the calculation of:

1. climate cost functions and

2. aircraft trajectories optimised on the basis of the climate cost functions,

where the climate cost functions (CCF) are specific climate metrics, i.e. climate impacts per unit emission. The idea of weather specific re-routing of air traffic for the benefit of climate has been addressed before (Sausen et al., 1994; Mannstein et al., 2005; Schumann et al., 2011; Sridhar et al., 2012). However, none of these studies included such a broad range of effects, as addressed in this study: contrails, carbon dioxide, ozone, methane, ozone from methane changes, water vapour. The changes in ozone arising from changes of its precursor methane are also called primary mode ozone (PMO).

The idea of REACT4C (Matthes, 2012; Matthes et al., 2012) is to first concentrate on frequently occurring daily weather patterns (Irvine et al., 2013), for which a detailed analysis is performed with a new modelling approach, which we describe here in detail. Results will be published in companion papers. The methodology is outlined in Fig. 1. As a first step, we are concentrating on the North Atlantic region, including most of Europe and North America. For this region a weather classification is performed taking into account specific air traffic routes (Irvine et al., 2013). For each type of weather pattern a representative weather pattern is selected. For this 1 day weather pattern, a grid is defined and for each grid point climate cost functions are calculated. For each grid point, which represents a certain region, we obtain in the end one value for the cost function with respect to one species. Since the weather situation changes during the day, the regions are temporally resolved. We refer to this as “time-regions”. The climate

GMDD
6, 4345–4416, 2013

cost functions are calculated with the chemistry–climate model EMAC (Version 2.42), which additionally includes two important submodels: ATTILA, a Lagrangian transport scheme (Reithmeier and Sausen, 2002) and AIRTRAC (Version 1.0, Frömming et al., 2013 in Supplement), calculating contributions from additional emissions to concentrations based on ATTILA. The EMAC submodel AIRTRAC is specifically developed for this study and described in Sect. 3. The determination of the climate cost functions (Fig. 1, left column highlighted box) includes first the calculation of the contributions of additional emissions to atmospheric concentrations and properties (nitrogen oxides, ozone, methane, contrails, water vapour, carbon dioxide), second the calculation of the radiative impact over a time period of weeks leading to an approximated annual mean instantaneous radiative forcing. Third, we use a correlation between instantaneous and adjusted radiative forcing to obtain the latter as a more reliable basis for the expected climate change (Sect. 3.4). This, eventually, is used as input to climate response formulas to obtain a set of metrics per unit emission, i.e. climate cost functions.

In Sect. 3.5 we relate individual metrics to political objectives and optimisation problems. The climate cost functions are used in the next step (Fig. 1) by a flight planning tool (SAAM) to obtain aircraft trajectories and respective emissions as well as the reduction in the climate impact due to the operational changes in aircraft trajectories. The climate cost function approach is aiming at reducing the contribution of air traffic on climate. The results for individual weather pattern can be multiplied by their frequencies to obtain an estimate of the total climate impact reduction as a result of the REACT4C re-routing strategy. Since this leads to changes in the background concentration and production efficiencies, e.g., ozone production per NO_x molecule, other emitter, such as industry or traffic, might have a larger climate impact (Grewe et al., 2012a). This can be investigated by applying chemistry–atmosphere models to obtain the total mitigation gain (Fig. 1, green boxes). This is planned in the project REACT4C, but not part of this publication (shaded box in Fig. 1).

The whole methodology is based on operational models, which are briefly introduced in Sect. 2 and it is based on new modelling approaches, which are described in detail

GMDD
6, 4345–4416, 2013

in Sect. 3 (climate cost functions). In Sect. 4 we provide a comparison to other studies and a sanity check of our modelling approach.

2 Base models

The REACT4C modelling approach is based on a number of models, which were applied previously many times. These models are combined with new approaches. Therefore we only briefly describe the base models and concentrate on a detailed description of the new approaches in Sect. 3.

2.1 Atmosphere: EMAC

The ECHAM/MESSy Atmospheric Chemistry (EMAC) model (here version 2.42) is a numerical chemistry and climate simulation system that includes submodels describing troposphere to middle atmosphere processes and their interaction with oceans, land, and human influences (Jöckel et al., 2006). Here we use the second version of the Modular Earth submodel System (MESSy2) to link the individual physical processes described in submodels (Jöckel et al., 2010).

The core model for the atmosphere is the 5th generation European Centre Hamburg general circulation model ECHAM5 (Roeckner et al., 2006). The chemistry is described by the submodel MECCA (Version 3.2) (Sander et al., 2011). More detailed information, including references, about the model system is available from http://www.messy-interface.org.

2.2 Aircraft routing and emissions

The simulation of the flow of air traffic is performed with the System for traffic Assignment and Analysis at a Macroscopic level (SAAM) to which the Advanced Emission Model (AEM) is coupled. An overview on the simulation system SAAM and AEM is given in Fig. 2 and discussed in more detail in Sect. 2.2.3.

GMDD
6, 4345–4416, 2013

2.2.1 SAAM

The integrated system SAAM, version 4.2.0 (Eurocontrol, 2012), is built for wide or local design, evaluation, analysis and presentation of air traffic airspace scenarios (http://www.eurocontrol.int/nm-services/saam-system-traffic-assignment-and-analysis-macroscopic-level). It allows to create, change and design air traffic route networks with their possible associated constraints (e.g. restrictions from the route availability document – RAD or flight level constraints). From any traffic demand (basically airport origin and destination, aircraft type and departure time), a set of full 4-D trajectories is generated.

The best choice of these 4-D trajectories is made using optimisation with an objective function minimizing a mathematical cost that can be based on economical values derived from flight time and aircraft operating cost, or based on the climate impact (see below). Constraints concerning conflict avoidance between all 4-D trajectories can be switched on or off in the optimisation model. Other optimisation models, for instance focusing on controlled sectors load balancing, were developed in SAAM (Champougny et al., 2001).

Aircraft performance included in SAAM uses Base of Aircraft Data (BADA) version 3.9 (see http://www.eurocontrol.int/services/bada), which also provide fuel flow based on aircraft-engine characteristics and assumption like mean aircraft load and weight.

2.2.2 AEM

The advanced emission model (AEM 2.5.0) has been developed to estimate the mass of fuel burnt, and emissions produced by a specific aircraft-engine configuration for a specific 4-D trajectory (Eurocontrol, 2013). Emissions are calculated for CO_2, H_2O, NO_x, SO_x, CO, unburned hydrocarbons (HC), benzene, and some other volatile organic compounds (VOCs) (see also http://www.eurocontrol.int/services/advanced-emission-model).

GMDD
6, 4345–4416, 2013

2.2.3 Application of SAAM with AEM

Figure 2 shows in more detail the information flow and coupling of SAAM and AEM. First, flights are selected from a database, including the city pair connection, departure time and aircraft. Second, routes are generated randomly. Here we apply a procedure, which generates alternative routes by blocking of air space areas in addition to a randomly changed cruise altitude. Three different grid sizes (Fig. 3) for the blocking of the air space were tested. The SAAM standard grid size (grid 0) leads to significant deviations from the great circle, whereas the smaller cells only provide small deviations. Hence, the resolution with the larger grid cells is better suited for a generation of alternative routes. This procedure leads to a randomly chosen variation of 16 additional routes in the horizontal with 4 additional options for the cruise altitude (3 below the original cruise level and one above) and hence 84 ($= 17 \times 5 - 1$) alternative routings for each city pair connection. The number of the blocked grid cells has been varied to test the sensitivity of this parameter to the optimisation process. We found that an increase in the number of blocked cells to 18 only shows a minor change in the optimal solution with differences well below 1 %.

The third step (Fig. 2) is the calculation of the 4-D trajectory, which includes a performance calculation and takes into account wind fields. This is followed by the fourth step, namely the calculation of the emissions by using the AEM model. This leads to a large set of trajectories. Based on these data an optimal air traffic flow is determined. The optimisation is either done with respect to economic or climate costs (climate impact). In the case of ignoring any conflicts, the optimisation simply chooses the minimum among the alternative routes for every city-pair connection. In the case of conflict avoidance, the routes depend on each other and a linear programming is applied:

GMDD
6, 4345–4416, 2013

$$\min \sum_{i,j} R_{ij} C_{ij} \tag{1}$$

subject to

$$\mathrm{CM}_{ijkl} \leq 0 \;\forall i,j,k,l \text{ conflict avoidance} \tag{2}$$

$$\sum_{i}^{n} R_{ij} = 1 \quad \forall j \quad \text{one route option per flight} \tag{3}$$

$$R_{ij} \in \{0,1\} \quad \forall i,j \quad \text{route option variable,} \tag{4}$$

with the flight index i (and k, respectively): $1 \leq i \leq n$ (n is the number of city pair connections), j (l respectively) the route option index (≤ 85, see above), the precalculated conflict matrix $\mathrm{CM} \geq 0$ (=number of conflicts) and the costs $C_{i,j}$. These costs are either defined for economic optimisation or climate optimisation. For economic optimisation the costs are

$$C_{i,j} = F_{i,j} C^{\mathrm{fuel}} + T_{i,j} C^{\mathrm{time}}, \tag{5}$$

with $F_{i,j}$ and $T_{i,j}$ the fuel consumption and flight time on route option (i,j) in [kg] and [min], respectively, and $C^{\mathrm{fuel}} = 0.75\,\mathrm{EUR\,kg^{-1}}$, $C^{\mathrm{time}} = 25\,\mathrm{EUR\,min^{-1}}$. For climate optimisation the costs are defined as:

$$\begin{aligned} C_{i,j} = \sum_{m} \Big[& M^{\mathrm{AiC}}(x_m)\ D_m \\ & + M^{\mathrm{O_3}}(x_m)\ N_m \\ & + M^{\mathrm{CH_4}}(x_m)\ N_m \\ & + M^{\mathrm{PMO}}(x_m)\ N_m \\ & + M^{\mathrm{H_2O}}(x_m)\ F_m \\ & + M^{\mathrm{CO_2}}(x_m)\ F_m \Big], \end{aligned} \tag{6}$$

GMDD
6, 4345–4416, 2013

where the flight trajectory of route option (i,j) is divided into flight legs with index m. Each flight leg has a center location x_m, a distance flown D_m [km], fuel consumption F_m [kg], and a NO_x emission N_m [kgN], which are multiplied with the respective climate cost functions with a certain metric M^{species} for the individual species (AiC is aircraft induced cloudiness, i.e. contrails and contrail-cirrus). See also next section for climate cost functions and metrics.

3 Methodology: climate cost functions

In this section we describe the calculation of the climate cost functions, starting with the Lagrangian approach, followed by the definition of the time-regions and the chemistry and microphysics of the atmospheric processes, radiation changes and the climate impact calculations. The atmospheric process modelling is performed in the EMAC submodels AIRTRAC and CONTRAIL. A further documentation of the program structure, subroutines and namelists is given in the Supplement.

3.1 A Lagrangian approach: tradeoff between computational efficiency and process accuracy

The calculation of climate cost functions requires a calculation for each of the predefined time-regions. Hence, the resolution of the climate cost function in time and space determines the number of climate cost function calculations. We denote the number of time-regions with N_{TR} and the individual time regions with TR_i $(i = 1, \ldots, N_{\text{TR}})$.

We chose a Lagrangian approach, since it allows to include a multitude of cost function calculations in a single EMAC simulation. Each trajectory is characterised by its position at any time and includes an arbitrary number of properties P. We assign for each time-region TR_i a set of n properties, i.e. $P((i-1)\cdot n+1), \ldots, P(i\cdot n)$. Figure 4 shows exemplarily for 5 time-regions (each coloured differently) a set of 8 properties,

GMDD
6, 4345–4416, 2013

namely the contribution of the emissions to the chemical species NO, NO_2, HNO_3, O_3, CH_4, and H_2O and contrail coverage (see Supplement for a complete list of the 13 (=`nlgtrac`) properties).

The Lagrangian approach is based on a detailed modelling of the background processes within EMAC and a – to some degree simplified – additional simulation of the contributions from emissions taking place in the respective time-regions (Fig. 5). Information from the detailed modelling is transferred to the trajectories and the contributions are calculated based on the results from the detailed process modelling within EMAC.

In principle two modelling approaches are applicable (1) the Lagrangian approach introduced above, (2) a perturbation approach, which includes a base case simulation and for each time-region an additional full simulation with the base model (here EMAC) including additional emissions from the time-region. Here we chose the Lagrangian approach since it better meets our objective: Obviously the Lagrangian approach has the advantage to be numerically efficient, since many time-regions are calculated in parallel. It further calculates the contribution of an emission in the time-region and separates it from compensating effects through changes in contribution from other sectors caused by non-linear processes, e.g. chemical saturation effects. On the other hand, the processes for the calculation of the time-region contributions are less detailed than the representation of the background processes in the base model EMAC.

The overall objective of our modelling approach is to minimise the contribution of air traffic to climate change. It is important to stress that the contribution calculation (Grewe et al., 2010) is much better suited to address this objective than the perturbation method, since it does not lead to misinterpretations of the results due to non-linear compensation effects in the chemistry (Grewe et al., 2012a).

Changes from the time-region emissions do not feedback to the base model processes (Fig. 5). This ensures an identical background meteorology and chemistry for all time-region simulations, i.e. we perform quasi chemical transport model (QCTM) simulations (Deckert et al., 2011).

GMDD
6, 4345–4416, 2013

The second approach, perturbation simulations for each time-region, would have the advantage of having the same degree of detailedness in the description of background processes and the perturbation. However, it is extremely time and resource consuming, the contribution of the time-region is not calculated, but only the total impact (see above and also Grewe et al., 2010, 2012a; Grewe, 2013).

3.2 Time-regions and emissions

3.2.1 Definition

Figure 6 shows the horizontal grid for the climate cost functions, covering the North Atlantic region for the area, where the optimisation with SAAM is performed (see Sect. 2.2.3). It consists of 6 longitudes, 7 latitudes and 4 pressure levels for three points in time (see Table 1 for details). This comprises 504 grid points, i.e. 504 calculations for the impact of emissions on the atmosphere have to be performed to provide a dataset. We take into account water vapour emissions and nitrogen oxide emissions (see Table 2). The emissions are released for one time-step (15 min) in the EMAC grid-box, in which the respective climate cost function grid point is located. Additionally, we consider properties of conventional present-day aircraft and fuel, such as the aircraft's overall propulsion efficiency, the combustion heat, and the water vapour emission index (see Table 2).

For each climate cost function grid point, emissions are partitioned on 50 trajectories, which are randomly distributed in the EMAC grid box in which the climate cost function grid point is located. Technically this is handled via the submodel TREXP and controlled by a namelist (Jöckel et al., 2010).

3.2.2 Sensitivity to the number of trajectories

Here we investigate the number of trajectories at each emission point that are required to obtain unambiguous results. If the number of trajectories is too low, only a few pos-

GMDD
6, 4345–4416, 2013

sible paths for the air parcels, carrying the emission, will be considered, and thus the results can become very noisy and random.

For this sensitivity study, 50 trajectories were released at each of the 24 emission points, located at 200 hPa at 45° N and 50° N and at 400 hPa at 40° N and 35° N. For each of the emission points, the mean NO_x (= NO + NO_2) mixing ratio over the first month of integration (i.e., January) was calculated over all 50 trajectories. We tested how strongly the results differ when less (between 2 and 48) trajectories were released. For each number of trajectories (between 2 and 48) 100 sub-samples out of the total 50 trajectories were randomly generated. For each sub-sample, the mean NO_x mixing ratio was calculated and compared to the mean over all 50 trajectories. The relative deviations for these sub-samples as a function of number of trajectories is shown for one emission point in Fig. 7 (top, left). Mean NO_x values differ by up to 40 % from the result for all 50 trajectories, if only 2 trajectories were used. With an increasing number of trajectories, the deviations decrease and converge towards the mean value over 50 trajectories. The same diagnostic is shown for the corresponding mean ozone mixing ratios (Fig. 7, upper right). It shows a similar behaviour as NO_x, but with a smaller initial spread in the results for small numbers of trajectories. In the bottom panel of Fig. 7, the standard deviation as a function of the number of trajectories shows a sharp decrease of the NO_x and ozone standard deviation from around 20 % to 5 % and 12 % to 4 % up to a trajectory number of around 20, respectively. This figure confirms that the deviation in the results of ozone is smaller than in the NO_x values also for the mean over the 24 emission points at different locations. While the mean standard deviation of the results is almost 20 % for NO_x and 12 % for ozone when using only 2 trajectories, it drops quickly with an increasing number of trajectories and both the mean values and the extremes lie below 10 % for more than 20 trajectories. Thus, this analysis suggests that the potential error in the results for NO_x and ozone almost converged for 50 trajectories and is lower than 10 % if 20 or more trajectories are used.

GMDD
6, 4345–4416, 2013

3.2.3 Sensitivity to temporal and horizontal resolution

We have tested the impact of the temporal and horizontal resolution on the climate cost functions. For the test of the temporal resolution, we included an emission time at 09:00 UTC in addition to the standard emission times at 06:00 UTC and 12:00 UTC at 250 hPa and between 45° N and 50° N. The interpolated values are compared to the simulated 09:00 UTC values. The NO_x and ozone masses vary by roughly ±40 % and ±25 %.

Concerning the horizontal resolution we have added emission locations in between the chosen grid, i.e. a latitudinal shift of 2.5° and longitudinal shift of 7.5° at 250 hPa and 12:00 UTC. The results show a variability in the order of 50 % and 35 % for NO_x and ozone, respectively.

Hence the horizontal interpolation is more critical than the temporal interpolation. The intercomparison further shows that the resolution of the climate cost function is crucial to the optimisation of the air traffic system with respect to its climate impact. However, the variation of the climate impact from NO_x emissions varies by one order of magnitude and is hence larger than the possible interpolation error.

3.3 Atmospheric changes

3.3.1 Chemistry: NO_x, O_3 (+PMO), OH, CH_4

We consider a NO_x emission of 5×10^5 kg in each time-region. This influences ozone production and destruction as well as the HO_x partitioning and hence methane depletion.

From the detailed modelling in EMAC, we obtain relevant production and loss terms. Those are then used in the following tagging approach. A pre-requisit of this tagging approach is a complete and disjunct partitioning of the emissions into categories. Here we consider two emission categories, a background (b) and the additional emission (e) for calculation of the climate cost function. For this emission category e the contribution

GMDD
6, 4345–4416, 2013

of this category to the ozone production is considered via, e.g., the reaction:

$$HO_2 + NO \longrightarrow OH + NO_2 \quad \text{(R1)}$$

is (according to Grewe et al., 2010):

$$P^{e}_{O_3} = P^{b}_{O_3} \cdot \frac{1}{2}\left(\frac{HO^{e}_{2}}{HO^{b}_{2}} + \frac{NO^{e}}{NO^{b}}\right), \quad (7)$$

where the superscripts *b* and *e* indicates background values and values specific for the tagged emission category, respectively. P_{O_3} denotes the ozone production rate in [mol mol^{-1} s^{-1}]. All species are given in mixing ratios [mol mol^{-1}]. The reaction rate for loss terms of tagged species is determined in the same manner, e.g. for the reaction

$$NO_2 + O_3 \longrightarrow NO + 2O_2 \quad \text{(R2)}$$

the loss term $L^{e}_{O_3}$ is

$$L^{e}_{O_3} = L^{b}_{O_3} \cdot \frac{1}{2}\left(\frac{NO^{e}_{2}}{NO^{b}_{2}} + \frac{O^{e}_{3}}{O^{b}_{3}}\right). \quad (8)$$

Note that the first term in brackets includes the depletion of background ozone by NO^{e}_{2} and that equations (7) and (8) just represent the contributions from an emission e for the reactions (R1) and (R2) without any further assumptions, e.g., without any linearisation of chemical processes.

For our approach we now introduce simplifications. First we combine background species to families and calculate the contributions of time-region emissions according to this family concept, with the assumption that the emissions are small enough that the specific reaction rates are unchanged, i.e.:

$$\frac{P^{b}_{O_3}}{HO^{b}_{2} \cdot NO^{b}} = \frac{P^{b}_{O_3} + P^{e}_{O_3}}{(HO^{b}_{2} + HO^{e}_{2})(NO^{b} + NO^{e})} \quad (9)$$

GMDD
6, 4345–4416, 2013

Further, we regard the ozone production as primarily NO_x dependent and split the ozone destruction into two parts driven by two different chemical families: one based on NO_x the other taking into account all other loss processes, which leads to the following differential equation for ozone:

$$\frac{\mathrm{d}}{\mathrm{d}t}O_3^e = \frac{P^b_{O_3}}{NO_x^b}NO_x^e - \frac{1}{2}D^b_{O_3,1}\left(\frac{NO_x^e}{NO_x^b} + \frac{O_3^e}{O_3^b}\right) - D^b_{O_3,2}\frac{O_3^e}{O_3^b} \quad (10)$$

This includes implicitly the assumption that the NO to NO_2 ratio of the NO_x emitted in the time-region is equal to the ratio of the background NO_x. After NO_x is emitted, we take into account an exchange with HNO_3^e, which eventually will be washed out.

Figure 8 shows an example for an emission at 200 hPa, 30° N and 75° W the evolution of the contributions to the atmospheric burden [kg] of varies species. Nitrogen oxides are totally washed-out within a month. Ozone increases as long as enough NO_x molecules are available and then it is destroyed.

An analogous approach is used for methane. We take into account the most relevant reactions regarding the concentration of OH and HO_2: production of OH:

$$H_2O + O^1D \longrightarrow 2OH \quad (R3)$$

$$HO_2 + O_3 \longrightarrow OH + 2O_2 \quad (R4)$$

$$HO_2 + NO \longrightarrow OH + NO_2 \quad (R5)$$

Loss of OH:

$$OH + O_3 \longrightarrow HO_2 + O_2 \quad (R6)$$

$$OH + CO \xrightarrow{O_2} HO_2 + CO_2 \quad (R7)$$

$$OH + RH \xrightarrow{O_2} RO_2 + H_2O \quad (R8)$$

$$OH + CH_4 \longrightarrow CH_3O_2 + H_2O \quad (R9)$$

$$OH + HO_2 \longrightarrow H_2O + O_2 \quad (R10)$$

GMDD
6, 4345–4416, 2013

Production of HO_2 in addition to (R6) and (R7):

$$RO_2 + NO \longrightarrow HO_2 + R'CHO + NO_2 \quad \text{(R11)}$$

Loss of HO_2 in addition to (R4),(R5) and (R10):

$$RO_2 + HO_2 \longrightarrow ROOH + O_2 \quad \text{(R12)}$$

$$HO_2 + HO_2 \longrightarrow H_2O_2 + O_2 \quad \text{(R13)}$$

We are not considering aircraft contributions for H_2O, CO, RH and CH_4 for this approach, since their effects on OH are considered to be small. The production and loss of OH^e, i.e. OH of the respective emission category, follows in analogy to Eq. (7):

$$P^e_{OH} = P^b_{R3}\frac{O^e_3}{O^b_3} + \frac{1}{2}P^b_{R4}\left(\frac{HO^e_2}{HO^b_2} + \frac{O^e_3}{O^b_3}\right) \quad (11)$$

$$+\frac{1}{2}P^b_{R5}\left(\frac{HO^e_2}{HO^b_2} + \frac{NO^e_x}{NO^b_x}\right) \quad (12)$$

and

$$D^e_{OH} = \frac{1}{2}D^b_{R6}\left(\frac{OH^e}{OH^b} + \frac{O^e_3}{O^b_3}\right) \quad (13)$$

$$+D^b_{R7}\frac{OH^e}{OH^b} + D^b_{R8}\frac{OH^e}{OH^b} + D^b_{R9}\frac{OH^e}{OH^b} \quad (14)$$

$$+\frac{1}{2}D^b_{R10}\left(\frac{OH^e}{OH^b} + \frac{HO^e_2}{HO^b_2}\right) \quad (15)$$

GMDD
6, 4345–4416, 2013

We derive in analogy the production and loss terms for HO_2^e and obtain differential equations for OH^e and HO_2^e, which easily can be solved as follows:

$$\frac{d}{dt}OH^e = P^e_{OH} - D^e_{OH} \tag{16}$$

$$= A_0 + A_1\frac{HO_2^e}{HO_2^b} + A_2\frac{OH^e}{OH^b} \tag{17}$$

$$= 0 \tag{18}$$

$$\frac{d}{dt}HO_2^e = P^e_{HO_2} - D^e_{HO_2} \tag{19}$$

$$= B_0 + B_1\frac{HO_2^e}{HO_2^b} + B_2\frac{OH^e}{OH^b} \tag{20}$$

$$= 0 \tag{21}$$

$$OH^e = OH^b\frac{A_0B_1 - A_1B_0}{A_1B_2 - A_2B_1} \tag{22}$$

$$HO_2^e = HO_2^b\frac{A_2B_0 - A_0B_2}{A_1B_2 - A_2B_1} \tag{23}$$

with

$$A_0 = \left(P^b_{R3} + \frac{1}{2}P^b_{R4} - \frac{1}{2}D^b_{R6}\right)\frac{O_3^e}{O_3^b} + \frac{1}{2}P^b_{R5}\frac{NO_x^e}{NO_x^b} \tag{24}$$

$$A_1 = \frac{1}{2}\left(P^b_{R4} + P^b_{R5} - D^b_{R10}\right) \tag{25}$$

$$A_2 = -\frac{1}{2}D^b_{R6} - D^b_{R7} - D^b_{R8} - D^b_{R9} - \frac{1}{2}D^b_{R10} \tag{26}$$

$$B_0 = \frac{1}{2}\left(D^b_{R6} - P^b_{R4}\right)\frac{O_3^e}{O_3^b} + \left(P^b_{R11} - \frac{1}{2}P^b_{R5}\right)\frac{NO_x^e}{NO_x^b} \tag{27}$$

GMDD
6, 4345–4416, 2013

$$B_1 = -\frac{1}{2}P^{b}_{R4} - \frac{1}{2}P^{b}_{R5} - \frac{1}{2}D^{b}_{R10} - P^{b}_{R12} - P^{b}_{R13} \quad (28)$$

$$B_2 = \frac{1}{2}D^{b}_{R6} + D^{b}_{R7} - \frac{1}{2}D^{b}_{R10} \quad (29)$$

The methane depletion caused by the contribution of aircraft emissions to the OH concentration is then

$$D^{e}_{CH_4} = D^{b}_{R9}\frac{OH^{e}}{OH^{b}} = D^{b}_{R9}\frac{A_0B_1 - A_1B_0}{A_1B_2 - A_2B_1}. \quad (30)$$

Figure 8 shows, in addition to NO_x and O_3, the evolution for methane. Methane decreases first because of an increase in OH via reaction (R1). When NO_x is removed from the atmosphere, the increase in ozone concentrations leads to an enhanced methane reduction.

3.3.2 Aircraft induced cloudiness

Contrails form in the atmosphere, when the ambient air at flight levels is sufficiently cold and moist (Schmidt–Appleman criterion, SAC; Schumann, 1996). Once formed, contrails may persist, if the air is supersaturated relative to ice and evolve into contrail-cirrus, i.e. they lose their line-shaped structure. Here we generally refer to contrails and do not distinguish between line-shaped contrails and contrail-cirrus.

We determine the atmospheric ability to form persistent contrails, i.e. the potential contrail coverage, instantaneously within the climate model at each time step following the approach of Burkhardt et al. (2008) and Burkhardt and Kärcher (2009). The potential contrail coverage, b_{co}, is the fraction of an EMAC grid box, which can be covered maximally by contrails. It is calculated as the difference between the maximum possible coverage of both contrails and cirrus (b_{co+ci}), and the coverage of natural cirrus alone

GMDD
6, 4345–4416, 2013

(b_{ci}):

$$b_{co} = b_{co+ci} - b_{ci}, \quad \text{with} \tag{31}$$

$$b_{ci} = 1 - \sqrt{\frac{r - r_{ci}}{r_{sat} - r_{ci}}}, \quad \text{and} \tag{32}$$

$$b_{co+ci} = \begin{cases} \frac{r - r_{co}}{r_{sat} - r_{ci}} - b_{ci}(1 - b_{ci}) & \text{for} \quad r_{co} \le r \le r^* \\ 1 & \text{for} \quad r > r^* \end{cases} \tag{33}$$

r denotes the grid mean relative humidity. r_{ci} and r_{co} are critical relative humidities above which a fraction of the grid box is covered by cirrus and is ice supersaturated, respectively; $r_{sat} = 1$ is the relative humidity at saturation. The relative humidity $r^* = r_{sat} - (r_{ci} - r_{co})^2/(r_{sat} - r_{ci})$ (see Burkhardt et al. (2008) and Supplement therein).

The critical relative humidity for contrail formation, r_{co} is calculated via

$$\frac{r_{co}}{r_{ci}} = \frac{r_{SAC}}{a\, r_{nuc}}, \tag{34}$$

with r_{SAC} being the relative humidity over ice at which the Schmidt–Appleman-criterion is fulfilled during the mixing of aircraft exhaust gases and ambient air, r_{nuc} is the homogeneous freezing threshold. As contrails often form prior to the formation of natural cirrus $a = 0.9$ is chosen (following Burkhardt et al., 2008).

The potential contrail coverage is transferred to the Lagrangian trajectories. Then the actual contrail coverage is calculated, depending on whether air traffic is actually taking place in the respective grid box. Further physical processes like contrail spreading, sedimentation of ice particles, water uptake and sublimation are parameterised. Contrails are described by their coverage (b) and water mixing ratio (m):

The prognostic equation for the contrail coverage is the sum of newly formed contrails and the spreading of already existing:

$$\frac{db}{dt} = \left(\frac{db}{dt}\right)_{new} + \left(\frac{db}{dt}\right)_{spread}, \tag{35}$$

GMDD
6, 4345–4416, 2013

with the boundary conditions that the resulting contrail coverage b fulfils:

$$b \leq b_{co} \tag{36}$$

$$b = 0 \quad \text{for} \quad m < m_{thres}. \tag{37}$$

The newly formed contrails cover an area depending on the initial contrail dimensions, such as the width W_0 and the length of the contrail in the grid box (D, see also Table 3). We assume a flown distance

$$D = \sqrt{A}, \quad \text{and hence an initial contrail length of} \tag{38}$$

$$L = D\, b_{co}. \tag{39}$$

A is the gridbox area. The resulting new contrail coverage tendency is then

$$\left(\frac{db}{dt}\right)_{new} = \frac{W_0\, L}{A\, \Delta t} = \frac{W_0\, b_{co}}{\sqrt{A}\, \Delta t}. \tag{40}$$

The spreading of the contrails is parameterised according to Burkhardt and Kärcher (2009) depending on the vertical wind shear:

$$\left(\frac{db}{dt}\right)_{spread} = c\sqrt{\left(\frac{\partial u}{\partial z}\right)^2 + \left(\frac{\partial v}{\partial z}\right)^2}\,\frac{H\, L}{A} \tag{41}$$

The prognostic equation for the contrail ice mass mixing ratio m includes the formation of new contrails, sedimentation (or precipitation) of ice mass, deposition of water vapour on the contrail ice particles and sublimation (Burkhardt and Kärcher, 2009):

$$\frac{dm}{dt} = \left(\frac{dm}{dt}\right)_{new} + \left(\frac{dm}{dt}\right)_{sed} + \left(\frac{dm}{dt}\right)_{dep/subl}. \tag{42}$$

Similar to Ponater et al. (2002) we assume that the newly formed contrail ice water mixing ratio depends on the condensation rate in the contrail covered part of the grid

GMDD
6, 4345–4416, 2013

box c_{co}, which is defined analogously to the condensation rate for natural clouds c_{cl}:

$$\left(\frac{dm}{dt}\right)_{new} = c_{cl}. \quad (43)$$

Extending over Ponater et al. (2002), however, contrail ice is also subject to physical sinks: The sedimentation rate of ice particles in the contrail is parameterised according to Heymsfield and Donner (1990) based on the vertical divergence of the flux of ice particles F in [kg m^{-2} s^{-1}]:

$$\left(\frac{dm}{dt}\right)_{sed} = \frac{1}{\rho}\frac{dF}{dz}, F = vm\rho, v = \alpha(\rho m)^{\beta}, \quad (44)$$

where v is the falling velocity [m s^{-1}] of ice particles, which are parameterised with $\alpha = 3.29$ and $\beta = 0.16$.

The sublimation and growth is parameterised according to a relative decrease or an increase of the potential contrail coverage, resulting from a decrease or increase of the relative humidity, respectively:

$$\left(\frac{dm}{dt}\right)_{dep/subl} = \frac{1}{b_{co}}\frac{db_{co}}{dt}m = \frac{d\ln b_{co}}{dt}m. \quad (45)$$

3.3.3 H_2O and CO_2

For every time-region a water vapour emission is taken into account (Table 2). This emitted water vapour (H_2O in [mol mol^{-1}]) is transported via Lagrangian transport, like the other tracers. Only loss processes are considered:

$$\frac{dH_2O}{dt} = -\frac{pr}{H_2O^{tot}}H_2O, \quad (46)$$

GMDD
6, 4345–4416, 2013

where pr is the precipitation rate, i.e. the water vapour loss in [mol mol^{-1} s^{-1}] in the respective EMAC gridbox due to rain and snowfall and H_2O^{tot} the respective grid box total water vapour in [mol mol^{-1}].

Carbon dioxide emissions are assumed to lead to a well-mixed enhancement of the carbon dioxide mixing ratio, because of its long perturbation life time. The temporal evolution of the concentration change (decay) is given for a unit of fuel used $CO_2(t)$ in [kg(CO_2) (kg(fuel))$^{-1}$] following Fuglestvedt et al. (2010) and Forster et al. (2007):

$$CO_2(t) = EI_{CO_2} \sum_{i=0}^{3} a_i e^{-\frac{t}{\alpha_i}} \tag{47}$$

(see Table 4 for details).

3.4 Radiative forcing

In this section we provide a methodology to calculate radiative forcings, which will serve as an input to the climate metric calculations (Sect. 3.5). Since we are considering relatively short pulse emissions, previous approaches have to be adapted. For all species, except for contrails, we consider the adjusted radiative forcing (e.g., Hansen et al., 1997). For ozone this requires new considerations, which are presented in the following sections. For contrails the difference between instantaneous and adjusted radiative forcing is small (Marquart, 2003) and neglected here.

3.4.1 General approach for adjusted radiative forcing for ozone

Radiative forcing is the common metric to inter-compare the global mean impacts of various components contributing to total climate change. As emphasized in previous work (Hansen et al., 1997; Stuber et al., 2001), the so-called stratosphere adjusted radiative forcing (also known as the fixed dynamical heating approximation, Forster et al., 1997) is generally better a quantification than the instantaneous forcing for the climate

GMDD
6, 4345–4416, 2013

impact to be expected from an ozone perturbation near or above the tropopause. The basic equation is

$$\Delta T_{\text{surf}}^{\text{eq}} = \lambda \ \ \text{RF}_{\text{adj}}, \tag{48}$$

which relates the global mean stratosphere adjusted radiative forcing RF_{adj} in [W m^{-2}] linearly to the global mean equilibrium surface temperature response $\Delta T_{\text{surf}}^{\text{eq}}$ in [K]. RF_{adj} is the radiative imbalance (at the tropopause or at the top of the atmosphere) induced by the forcing perturbation, determined after the stratosphere has re-adjusted to thermal equilibrium. λ in [K (W m^{-2})$^{-1}$] is the climate sensitivity parameter which has been assumed, initially, to be a universal constant, independent of the nature or the distribution of the perturbation. If instead of RF_{adj} the instantaneous forcing RF_{inst} is used in Eq. (48), λ becomes strongly perturbation-dependent and even the sign of the radiative forcing may become inconsistent with the resulting surface temperature response in case of an ozone perturbation at higher altitudes (e.g. around 20 km) altitude (Hansen et al., 1997). The necessity to quantify perturbations in terms of RF_{adj} poses a specific problem for the methodology used in the present study: RF_{adj} cannot be calculated directly for a pulse perturbation, as such a perturbation is not stationary, meaning that the stratospheric temperature cannot adjust to a new equilibrium. In contrast, RF_{inst}, could easily be determined even in such a case, at any location of the parcel in space and time, as no temperature adjustment is needed for calculating the instantaneous radiative flux change induced by a changing absorber. Yet, because we regard each of our short-lived perturbations as part of aviation climate impact as a whole (when stratospheric temperature adjustment will be non-negligible), it has to be assessed by a metric consistent with RF_{adj}. In the following we will discuss a thought experiment that illustrates the problem. The general idea is to translate an instantaneous radiative forcing RF_{inst} resulting from a pulse emission into an equivalent stratosphere adjusted radiative forcing RF_{adj} by means of an analytical formula:

$$\text{RF}_{\text{adj}} = f_1(t) \times f_2(p) \times \text{RF}_{\text{inst}}, \tag{49}$$

GMDD
6, 4345–4416, 2013

The unitless functions f_1 and f_2 describe the relation between RF_{adj} and RF_{inst}, for various times of the year (f_1, seasonal cycle) and various perturbation altitudes (f_2) and are derived from additional idealised simulations.

3.4.2 Thought experiment

Let us assume we consider two alternative flight routings, implying emissions in two different time-regions. We want to answer the following question: "Which routing induces the lower climate impact?" Let us further assume we had the same meteorology every day. The constraint from this thought experiment is then that the decision on the preferable routing is identical every day.

We now investigate two different assessment approaches, which both should lead to the same choice of routing. Figure 9 shows (green) RF_{inst} of a short pulse emission, e.g. as originating from NO_x emissions of one individual flight. The pulse is short compared to the temperature adjustment time of the stratosphere and a temperature adjustment is not yet achieved. One can regard this period as a spin-up for RF_{adj}, during wich the adjusted and instantaneous RFs still are equal. Both RF_{inst} and RF_{adj} are positive in this case. A sequence of individual pulses (flights), occurring every 0.005 time units, will also lead to a positive, though higher, RF_{inst} (blue). In this case, however, the continuous sequence of pulses gradually induces stratospheric temperature adjustment, reducing RF_{adj} with respect to RF_{inst} over time until it gets, in this example which is geared to ozone effects, eventually negative (−2 RF units, magenta). Thus, the assessment of an individual flight as part of a sequence of the same flights, and with the same meteorology every day, has to reflect this negative RF. Its time developing radiative impact consists of contributions of varying strength and sign, and it contains an additional tail of negative values (red line). This contribution has to be included for the assessment of the flight in terms of its time averaged RF.

As mentioned, such an equivalent RF_{adj} cannot be gained directly from the individual pulse simulation. We overcome this dilemma by calculating a response function (Eq. 49) to obtain a parameterised RF_{adj}, transferring RF_{inst} to RF_{adj} by means of pre-

GMDD
6, 4345–4416, 2013

calculated temperature adjustment effects from various types of the pulse perturbation. The terms of the response functions can be obtained from idealised simulations that calculate RF_{adj} and the associated stratospheric temperature adjustment from a limited number of typical ozone perturbations located at various altitudes and latitudes, and under various conditions of insolation.

3.4.3 Simulation set-up

Three idealised ozone perturbation patterns (see Supplement) are considered, which were adopted from previous simulations evaluating a number of emissions, located in various latitude-height bands (Fichter, 2009). The NO_x emissions basic to the ozone patterns discussed here occurred at altitudes of 200, 160, and 130 hPa, within the Northern Hemisphere extratropics (see Supplement for more details). Radiative forcing calculations were performed with EMAC for each perturbation pattern over an 1 yr period, preceded by a 3 months spin-up for the adjustment of stratospheric temperatures. The simulations include a calculation of the adjusted as well as the instantaneous RF. Each of the 12 months is interpreted as an individual pulse, and the RF_{inst} and RF_{adj} that it induces can be directly compared from the simulation and difference between RF_{inst} and RF_{adj} can be determined for each calender month.

Additionally, we have extended the simulation by four simulations for the second year, where we have successively switched off the ozone perturbation after January, April, July and October. These simulations are used to quantify the contribution of the adjusted stratospheric temperatures to the RF calculations after the perturbation has faded out. As soon as the perturbation pattern is removed in the respective (second simulation) month, the only contribution to the RF arises from the remaining stratospheric temperature changes, which turn back to the unperturbed situation rather fast. It turned out that this contribution to RF_{adj} is only of minor importance, so that we could omit it for the sake of simplicity.

GMDD
6, 4345–4416, 2013

3.4.4 Separation of height and time dependencies

Figure 10a shows the seasonal cycle of the radiative forcing (both RF_{inst} and RF_{adj}) as caused by a NO_x pulse emission over one month (see Supplement for the respective ozone pattern). As explained in Sect. 3.4.3, RF_{adj} values imply the assumption that preceding emissions induced a stratospheric temperature adjustment before the considered pulse was initiated. A distinct annual cycle is obvious, reflecting the insolation variation that directly effects the shortwave component of the radiative forcing. The contribution of the stratospheric temperature adjustment to RF_{adj} displays a seasonal cycle, too, as heating due to solar absorption by stratospheric ozone forms an important component of the adjustment. There is a general increase of RF with the altitude of the pulse emission. For pulses emitted at 130 hPa and 160 hPa RF_{adj} is larger than RF_{inst}, whereas the opposite is true for an emission at 200 hPa.

Following our approach to derive a scaled instantaneous forcing serving as a proxy for RF_{adj}, we normalise all seasonal cycles to the respective August value (Fig. 10b). The ratio between these August reference values of RF_{adj} and RF_{inst} is 1.56, 1.18, and 0.97 for 130 hPa, 160 hPa, and 200 hPa, respectively. The relative time development becomes much more unique, and the normalised adjusted RF is always lower than the normalized instantaneous RF, allowing the rescaling of RF_{inst} to yield the required proxy RF_{adj} (eq. 49). The relative difference displays a clear seasonal cycle (Fig. 10c) with largest differences in winter (about 15 %), which can be approximated by a sine function (back line):

$$f_1(t) = f_1^{\text{mean}} \left[\sin\left(2\,\pi\,\frac{t-7.5}{12} + \frac{\pi}{2}\right) - 1 \right], \tag{50}$$

with $f_1^{\text{mean}} = 0.08$ being the amplitude describing the deviation of peak values at summer and winter from the mean and t being the month of the year. It is obvious from Fig. 10c that the approximation is largely independent from the emission altitude justifying the approach of decomposed functions in Eq. (49).

GMDD
6, 4345–4416, 2013

The altitude dependency of the relation between RF_{inst} and RF_{adj} can be described from the three examples in Fig. 10a (based on simulations by Fichter (2009) as mentioned) and five further perturbation examples of similar type previously evaluated by Stuber (2003). The fifth data point is at 50 hPa, hence out of the region of interest, but used for the fit forming the parameterisation. Note that the experimental designs of Fichter (2009) and Stuber (2003) are both Northern Hemisphere ozone changes at different altitudes, though they are differing in detail, especially for the prescribed ozone pattern. The results are displayed in Fig. 11. In cases where the ozone increase is located in the troposphere exclusively (i.e., below approximately 200 hPa), RF_{adj} is smaller than RF_{inst}, since the stratospheric temperature adjustment implies a cooling caused by the blanketing effect of the perturbation. In the tropopause region and in the lowermost stratosphere, an ozone increase induces a dipole-like stratospheric temperature adjustment, with warming by solar absorption where the stratospheric part of the perturbation peaks and cooling above. The cases are also characterised by a positive instantaneous forcing at the tropopause, with longwave and shortwave contributions adding constructively (for tropospheric ozone changes), or with the positive longwave contribution dominating over a negative shortwave contribution (lowermost stratosphere). In cases where the ozone increase takes place at even higher altitudes (between 150 and 50 hPa), RF_{inst} at the tropopause becomes negative, because the effect of shortwave absorption dominates the instantaneous longwave cooling (Hansen et al., 1997; Stuber et al., 2001). RF_{adj} continues to be positive, however, as the warming of the stratosphere by the absorption of the upwelling longwave radiation and downwelling shortwave radiation provides an additional downward longwave flux, which for lower tropospheric ozone perturbations is strong enough to overcompensate the instantaneous net effect. In those cases the ratio between RF_{adj} and RF_{inst} is negative (Stuber, 2003). The fit resembles the overall structure well:

$$f_2(p) = C - A\frac{Ep - D}{B(Ep - D)^2 + 1}, \tag{51}$$

GMDD
6, 4345–4416, 2013

with $A = 1.1$, $B = 2.0$, $C = 1.05$, $D = 3.4$, $E = 1/60$.

A summarising sketch is provided in Fig. 12: The instantaneous upward and downward net flux (net means sum of shortwave and longwave) are balanced (black arrows) in the unperturbed case (left). When introducing a tropospheric perturbation (second left, red line) the downward fluxes remain basically unchanged, but the upward longwave flux (and hence the upward net flux) is reduced. This instantaneous flux imbalance (green arrow) equals a positive instantaneous radiative forcing (green bar). This leads to a stratospheric cooling (blue line) and hence to a reduced downward longwave flux, shown as an upward net flux (blue arrow). The combination of the instantaneous radiative forcing and this flux change yields the adjusted radiative forcing, which is hence smaller than the instantaneous RF.

A perturbation near tropopause altitudes (second right, red line) is much more effective than a pure tropospheric perturbation, leading to a stronger flux imbalance (green arrow) and instantaneous RF (green bar). The adjusted stratospheric temperature, however, has a cooling and warming component (blue line) and may result in an additional longwave downward flux (blue arrow) and hence a larger adjusted RF than instantaneous RF. A pure stratospheric perturbation (right) leads to a reduced shortwave downward flux and hence a reduced net flux (black arrow). The instantaneous RF is therefore negative, while the resulting adjusted stratospheric temperatures are positive (blue line). This leads to a strong longwave downward flux (blue arrow), which overcompensates the flux imbalance (green arrow) and yields a positive adjusted RF.

3.4.5 Overview: calculation of RF for individual species

Table 5 gives an overview on the RF calculation for the individual species. The RF calculation for CO_2 is based on Fuglestvedt et al. (2010) and includes a simple linearised conversion factor between the change in its atmospheric mass and the RF of $1.82 \times 10^{-12}\,\mathrm{mW\,m^{-2}\,(kg(CO_2))^{-1}}$. The contrail RF is derived from the global mean

GMDD
6, 4345–4416, 2013

radiation flux changes F at the tropopause

$$\mathrm{RF}^{\mathrm{contrail}} = \frac{1}{T} \int_{t_0}^{t_0+T} F(t)\mathrm{d}t, \tag{52}$$

where $T=1$ yr. Ozone RF is calculated analogously, except that the adjusted RF is derived by using Eq. (49). Methane RF is derived from the methane mass changes calculated explicitely (Sect. 3.3.1) by applying the respective IPCC formula (Shine et al., 1990). PMO radiative forcing is derived from the methane radiative forcing by a constant factor of 0.29 (Dahlmann, 2012). Water vapour adjusted RF is calculated, based on results from Grewe and Stenke (2008, see Fig. 13). Grewe and Stenke (2008) investigated the consequences of sustained water vapour emissions at different atmospheric locations between the surface and 50 hPa and between the pole and the tropics. The results show that the adjusted RF depends on the lifetime of the perturbation and on a linear relationship between the atmospheric mass change and RF. Here, we calculate the mass change explicitely (Sect. 3.3.3) and use the mass–RF relationship (Fig. 13).

3.5 Climate metrics and emission scenarios for the REACT4C objective

We are aiming at minimizing the air traffic's climate impact by alternative routings. However, the wording "climate impact" or "climate change" is not well defined and incorporates a variety of possible interpretations. Hence, we clarify our objectives and derive from that adequate climate metrics and emission scenarios (Grewe and Dahlmann, 2012).

As discussed in Sect. 3.4.2, we aim at reducing the climate impact of air traffic by introducing a new routing strategy. That implies that this strategy is applied every day for air traffic. We interpret climate change as the global mean temperature change. The definition of the strategy and the focus on global mean temperature change as a climate change indicator implies an emission scenario and a climate metric (see Table 6): The

GMDD
6, 4345–4416, 2013

first question Q1 is "What is the *shortterm* climate impact of the REACT4C re-routing strategy?". The appropriate emission scenario is a best estimate for the future air traffic and the average temperature response for a 20 yr time horizon $H = 20$ is a suitable climate indicator.

$$\mathrm{ATRH} = \frac{1}{H} \int_{t_0}^{t_0+H} \mathrm{d}T(t)\mathrm{d}t. \tag{53}$$

Since estimates of the future air traffic are naturally uncertain, one can argue that a sustained emission is an adequate assumption. A third option is to replace the mean temperature change over the time horizon H by the temperature change at the time horizon H, i.e. the absolute global temperature potential AGTP20 (see Supplement and Fuglestvedt et al., 2010). And as a last option, with the assumption that the climate sensitivities are equal to $1\,\mathrm{K}\,(\mathrm{W\,m^{-2}})^{-1}$ for all species (see Eq. 48) the absolute global temperature potential for the time horizon $H = 20$ can be approximated by the integrated radiative forcing for a pulse emission, i.e. GWP20.

The second objective, i.e. Question Q2 is "What is the *longterm* climate impact of the REACT4C re-routing strategy?". It changes the focus from the near-future to longer term effects and hence the emission scenarios and metrics are the same as for Q1, except for the time horizon ($H = 100$).

For reasons of completeness, we add here question Q3: "What is the medium climate impact of a *today's* REACT4C re-routing decision?". Here, a medium ($H = 50$) time horizon of 50 yr is addressed, but more importantly only the today's routing change and not a change in the strategy is addressed. Hence a pulse emission in combination with ATR50 or AGTP50 is the adequate choice of the combination of emission scenario and metric.

The choice of the objective has a consequence on the importance of individual atmospheric processes (Table 6). From question Q1 to Q3 the focus shifts from short to long-term effects and hence from contrails and ozone impacts to CO_2, only.

GMDD
6, 4345–4416, 2013

4 Verification

We have set-up a complex modelling scheme, combining new methods in calculating the contribution of aviation on atmospheric processes with an air traffic model. A validation of this specific model application is not possible, since most of the effects are not yet measured or are per se not measurable, such as the effect of a local NO_x emission at 200 hPa on the temperature change after 50 yr. Instead, we compare our results with earlier modelling studies. Even this is extremely difficult, since the focus of these studies is different and no direct intercomparison is possible. Hence we are more focusing on the soundness of the data (sanity check) rather than a verification or validation.

4.1 Chemistry

We have computed climate cost functions for one specific day in December. The underlying weather pattern represents a strong zonal jet, which represents the winter pattern 1 according to Irvine et al. (2013). For each cost function gridpoint (see Table 1), the mean over all 50 trajectories is calculated. Figure 14 shows the temporal development of NO_x, ozone, H_2O and loss of CH_4 of these mean values for each cost function grid point.

A NO_x and ozone lifetime of 20 ± 11 days and 72 ± 26 days is calculated, respectively, which is roughly in agreement with findings by Stevenson et al. (2004), who found a decrease of a NO_x pulse emission from roughly 110 $Gg(NO_2)$ to 20 $Gg(NO_2)$ within a month, which represents a lifetime of approximately 25 days and a decrease of ozone from around 10 Tg to 1.5 Tg within 2 months representing a lifetime of approximately 50 days (see also Fig. 14). The temporal evolution of NO_x, ozone and methane changes for a January pulse emission calculated by Stevenson et al. (2004) (white lines in Fig. 14) is well within the range of our results.

The relation between the NO_x emission and ozone contribution as a mean over all grid points is $7.8 \pm 2.4\,DU(TgN\,a^{-1})^{-1}$. Dahlmann et al. (2011); Frömming et al. (2012) and Grewe et al. (2002) calculated values for the whole air traffic and annual emis-

GMDD
6, 4345–4416, 2013

sions of 1.4 DU TgN^{-1}, 0.8 DU TgN^{-1}, and 0.7 DU TgN^{-1} respectively. However, those studies consider a whole air traffic scenario, with a large contribution of emissions from lower altitudes and lower ozone impacts. In our study, the ratio between the NO_x enhancement and the ozone change is 2400 kg(O_3) per kg(N) with a range of 270 to 300 000 kg(O_3) per kg(N). Grewe et al. (2002) calculated a value of 300 kg(O_3) per kg(N); thus our result is again at the lower end for the same reason. The respective RF value is 41 mW m^{-2} DU^{-1} (this study) and compares well with 31 mW m^{-2} DU^{-1} calculated by Dahlmann et al. (2011). The emission specific ozone RF calculated here ranges from 15 to 2800 mW m^{-2} TgN^{-1} with a mean value of 250 mW m^{-2} TgN^{-1}. Dahlmann et al. (2011) and Fuglestvedt et al. (2008) give mean values for the whole air traffic of 41 mW m^{-2} kgN^{-1} and 45 mW m^{-2} kgN^{-1}, respectively, which are well in the simulated range.

The relation between the ozone and methane RF is in the range of −0.5 to −1.3. Lee et al. (2010) and Holmes et al. (2011) summarised previous model simulations and found relations which amount to -1.65 ± 0.36 and −1.70, respectively. However, these values refer to the global air traffic, whereas we consider here emissions in the upper troposphere and lower stratosphere of the Northern Atlantic region during winter. Grewe and Stenke (2008) give a value of around −1 at those altitudes and latitudes.

To summarize, the lifetime of simulated NO_x and O_3, the ratio between the NO_x emission and ozone contribution, the resulting specific RF and the ratio between the ozone and methane RF show large variabilities between the individual grid points of the climate cost function and values published in literature are well within this range.

The water vapour specific emission RF is 5.5×10^{-11} mW m^{-2} kg(H_2O)$^{-1}$) ranging from 0.5 to 20×10^{-11} mW m^{-2} kg(H_2O)$^{-1}$). For a fleet with 170 Tg of fuel use this leads to a RF of 12 mW m^{-2} with a range of 1–43 mW m^{-2}. Also here the value of Lee et al. (2010) of 3 mW m^{-2} is well within this range. The recent estimate by Wilcox et al. (2012) of 0.9 mW m^{-2} with a range of 0.3 to 1.4 mW m^{-2} is at the lower end of our extrapolation.

GMDD
6, 4345–4416, 2013

4.2 Contrails

A variety of studies have investigated the properties of contrails (Lee et al., 2010; Heymsfield et al., 2011). Observations cover contrails at the age of seconds to hours and were performed by in-situ measurement techniques and remote sensing, e.g. from satellite platforms. Here we focus on some climate relevant contrail properties, such as ice water content and optical depth in the visible spectral range and show a model-to-model radiative forcing benchmark test.

Both modelling and observational data vary by orders of magnitude (e.g., Kärcher et al., 2009; Schumann, 2012). In addition direct intercomparisons are often challenging for many reasons, like different environmental conditions, different sampling periods, and different detection limits. For example modelling studies often simulate a wide range of optical thickness of contrails, which, e.g. cannot be detected from satellite (Marquart et al., 2003; Kärcher et al., 2009). Forall this reasons, the comparison of contrail properties such as ice water content and optical thickness for a limited number of simulations, can just be seen as a sanity check rather than a hard benchmark test (Grewe et al., 2012b).

Figure 15a shows observed and simulated ice water content in contrails as a cummulative probability density function. In-situ measurements from Voigt et al. (2011) (blue) and Schröder et al. (2000) (green) include 14 and 12 contrails, respectively, but nevertheless show a large variability. Our simulations (88 regions of contrail formation, red) cover a similar range and show a similar distribution as Voigt et al. (2011). Kärcher et al. (2009) simulated a wide range of environmental conditions for contrail formation and found in their modelling study a median ice water content of 0.6 $\mathrm{mg\,m^{-3}}$, which is close to our results of 0.2 $\mathrm{mg\,m^{-3}}$.

Note that the location and time of the year differ in these studies. Data from Voigt et al. (2011) are obtained at 220 to 300 hPa in central Europe in November and Schröder et al. (2000) include data in the altitude range from 300 to 200 hPa also over central Europe, but in April/May and October, whereas here, we investigate simulated contrail

GMDD
6, 4345–4416, 2013

properties from 200 to 400 hPa over the North Atlantic in December. We find 88, out of 504, situations where contrail form and take values of ice water content and optical properties when the contrail is fully evolved. In addition, the sampling frequency and representativity of the data with respect to the contrail area largely differs between the studies.

The cummulative probability density function of the contrail optical depth for wavelengths in the visible of these are presented in Fig. 15b. Satellite measurements (Iwabuchi et al., 2012), deviate enforcedly from in-situ measurements, such as Voigt et al. (2011) and modelling studies such as Kärcher et al. (2009); Frömming et al. (2011), because they cannot detect subvisible or thin contrails, let alone that the sampling periods and areas are substantially different. In general, we find for our specific simulated day smaller optical depths than the studies by Kärcher et al. (2009) and Frömming et al. (2011), which cover a much broader range of environmental parameters. Kärcher et al. (2010) compared simulated optical depths with a cloud model for the United States and found a median optical depth of 0.02, which is closer to our simulated median optical depth.

We performed the RF-contrail benchmark test by Myhre et al. (2009), where a globally uniform 1 % contrail coverage with an optical depth of $\tau = 0.3$ in the visible spectrum at 11 km, is prescribed. The results are shown in Fig. 16 and 17. EMAC and ECHAM4 (E4) fall well within the variability of the all models (for details on this test for E4 see Frömming et al., 2011). EMAC has an increased number of spectral interval compared to E4: 4 and 16 bands in the short- and longwave, compared to 2 and 6, respectively. The difference in the long-wave part of the RF between E4 and EMAC is small, but it differs significantly for the short-wave net forcing. However, both models are well within the overall range, which is encouraging, as four of the five radiative transfer models of Myhre et al. (2009) are much more sophisticated than the simplified schemes that have to be used in 3-D models.

GMDD
6, 4345–4416, 2013

4.3 Metrics

Here we compare the results for the most common climate metrics (AGWP20, AGWP100 and AGTP50) for ozone and methane (see Sect. 3.5) with results presented in Fuglestvedt et al. (2010). They analysed the GWP and GTP of ozone and methane (i.e. the AGWP and AGTP of ozone and methane normalised with the related AGWP and AGTP of CO_2) for different time horizonts for a 1 yr pulse emission of NO_x. We normalise the values with the respective metric for CO_2 (Table 7) to obtain the respective GWP and GTP values. For all metrics the ozone values are well within the range of previous studies. As already reported in Sect. 4.1, the regarded region (mid to high latitudes in the tropopause region) is characterised by a stronger methane depletion per ozone enhancement than for the whole air traffic (Grewe and Stenke, 2008). Hence the methane metric values are at the lower end of the values reported in Fuglestvedt et al. (2010).

4.4 Aircraft trajectory

Figure 18 shows for one city pair connection (Washington to Vienna) various flight options. The flight on that day (light brown) clearly follows the jet stream (arrows). We have performed an optimisation of the whole transatlantic air traffic with respect to short-term climate impacts (question Q2 in Table 6, with option 3 GWP20) with respect to costs and obtain for this city pair (blue) a different trajectory, which follows more closely the jet stream. However, when the traffic is cost-optimised and icludes conflict avoidance, as in reality, then the real route (light brown) and the cost-optimal (cheapest) route within a conflict-free traffic (dark brown) are much closer. The difference in distance and time is around 1 % and in fuel about 3 %.

For this city pair, the climate optimal routes (with and without conflict avoidance) with respect to short-term climate impact (see above) are located further North and at lower flight altitudes (FL330 and FL310). The conflict free climate optimised route (green) avoids more contrails and leads to a decrease in contrail AGWP20 by 16 %

GMDD
6, 4345–4416, 2013

and a decrease in NO_x AGWP20 by 4 % with an increase in fuel consumption by 14 %, which relates to an increase in GWP20 from CO_2 by 1 %.

This is one essentially random example, for a particular weather pattern, a particular city pair and a particular choice of climate metric. No general conclusions can be drawn from this one example, beyond the fact that "climate friendly" routes can indeed differ from the least-cost routes. It is the aim of REACT4C to produce a more systematic analysis across weather conditions and metrics.

5 Conclusions

We have developed a simulation framework for investigating climate change mitigation options for air traffic routing by avoiding climate sensitive regions. It includes three major steps: the calculation of climate cost functions, the simulation and optimisation of air traffic according to these climate cost functions and the estimate of the total mitigation gain. The climate cost functions describe the air traffic's contribution to climate change, which is caused by an emission at a certain time and location in the atmosphere. The processes we are regarding are ozone formation, methane loss, methane-induced ozone change, contrails (including the spread into cirrus), water vapour and carbon dioxide.

The simulation of physical processes is described using the chemistry–climate model EMAC, which we extended by two submodels AIRTRAC and CONTRAIL. They are described in detail in the Supplement (Frömming et al., 2013). By using the Lagrangian transport scheme ATTILA, we were able to simulate a climate cost function at a multitude of gridpoints in one simulation. We used state-of-the-art chemistry and microphysics for the simulation. New is the way how the model is used and how the climate cost functions are calculated, which required a couple of new considerations, e.g. regarding the calculation of the radiative forcing. We developed a parameterisation, which relates the radiation changes caused by a 15 min pulse emission to an adjusted radiative forcing.

GMDD
6, 4345–4416, 2013

We used one specific simulated day in December, which was characterised by a strong zonal jet stream over the Atlantic. We calculated the 4-D climate cost function dataset and optimised the cross-Atlantic air traffic with respect to economic costs and climate impact. Unfortunately a validation is hardly possible, since observational data for relations between emissions at flight altitude and climate impact is not available. Instead, we performed a sanity check of our calculated data and compared our results to previous studies, knowing that the comparison is very crude. In detail, we compared our calculated contribution of an emission at a very specific location and time to published results based on global and mostly annual air traffic emissions. Nevertheless, the ranges of e.g., contribution of NO_x emissions to ozone and RF, contrail properties etc., compare well with values from the literature.

It is important to note that uncertainties are associated with the calculation of the climate cost functions. For the optimisation, the absolute values of the climate costs are less important. More important is the relation of the climate impact of individual components and the spatial and temporal variability. In general, the uncertainty of a mean value and of any sensitivity are not necessarily correlated. Stevenson et al. (2006) showed in a multi model intercomparison that the simulated ozone burden and methane lifetime have quite some variability, but the models are very consistently simulating sensitivities. Grewe and Dahlmann (2012) intercompared results of the effect of flight altitude changes to ozone, water vapour and contrails based on Grewe and Stenke (2008); Köhler et al. (2008) and Rädel and Shine (2008) and found similar sentivities for ozone and contrails, but larger for water vapour and methane.

The calculated climate cost functions will form the basis for a detailed analysis of the climate change mitigation potential of the air traffic system. First results indicate that already today a large potential exists to reduce the contribution of air traffic to anthropogenic climate change significantly. In future publications we will investigate this potential in more detail. The optimisation with respect to climate might be an extreme scenario. Nonetheless, already small changes to the air traffic system, i.e. the change of a few very climate sensitive flights might already yield a large reduction of the air

GMDD
6, 4345–4416, 2013

traffic's climate impact, through reduction of contrail and NO_x effects with only small increases in fuel consumption. However, such conclusions are influenced greatly by the overall objective, or in other words the aim of any climate change policy, which in turn controls the choice of the climate emission metric and the choice of time horizon for those metrics. Some choices would put a greater value on reducing the forcing due to short-lived components such as contrails and NO_x, whilst others would put a greater value on reducing the forcing due to the longer-lived emissions, notably CO_2.

Supplementary material related to this article is available online at http://www.geosci-model-dev-discuss.net/6/4345/2013/gmdd-6-4345-2013-supplement.zip.

Acknowledgements. This work was supported by the European Union FP7 Project REACT4C (React for climate: http://www.react4c.eu/). We greatfully acknowledge DKRZ, where the simulations were performed under project bd0718. We thank Robert Sausen for the initiation and support of this project and Ulrike Burkhardt for discussions concerning the simulation of contrail-cirrus and Christiane Voigt for providing CONCERT data.

The service charges for this open access publication have been covered by a Research Centre of the Helmholtz Association.

References

Berntsen, T. and Fuglestvedt, J.: Global temperature responses to current emissions from the transport sector, P. Natl. Acad. Sci. USA, 105, 19154–19159, 2008. 4347

Burkhardt, U. and Kärcher, B.: Process-based simulation of contrail cirrus in a global climate model, J. Geophys. Res., 114, D16201, doi:10.1029/2008JD011491, 2009. 4347, 4363, 4365

Burkhardt, U. and Kärcher, B.: Global radiative forcing from contrail cirrus, Nature Climate Change, 1, 54–58, doi:10.1038/nclimate1068, 2011. 4347

GMDD
6, 4345–4416, 2013

Burkhardt, U., Kärcher, B., Ponater, M., Gierens, K., and Gettleman, A.: Contrail cirrus supporting areas in model and observations, Geophys. Res. Lett., 35, L16808, doi:10.1029/2008GL034056, 2008. 4363, 4364

Champougny, T., Duchene, A., Joubert, A., Lambert, J., and Minoux, M.: SOP: a decision-aid tool for Global Air Traffic Management System Optimisation, 4th ATM Seminar – Santa Fe, NM, USA, December, 2001, available at: http://atmseminar.eurocontrol.fr/past-seminars/4th-seminar-santa-fe-nm-usa-december-2001/papers/paper_132/view (last access: August 2013), 2001. 4351

Dahlmann, K.: Eine Methode zur effizienten Bewertung von Maßnahmen zur Klimaoptimierung des Luftverkehrs, Dissertation, DLR-Forschungsbericht, DLR-FB-2012-05, 134 p., 2012. 4374, 4395

Dahlmann, K., Grewe, V., Ponater, M., and Matthes, S.: Quantifying the contributions of individual NO_x sources to the trend in ozone radiative forcing, Atmos. Environ., 45, 2860–2868, doi:10.1016/j.atmosenv.2011.02.071, 2011. 4376, 4377

Deckert, R., Jöckel, P., Grewe, V., Gottschaldt, K.-D., and Hoor, P.: A quasi chemistry-transport model mode for EMAC, Geosci. Model Dev., 4, 195–206, doi:10.5194/gmd-4-195-2011, 2011. 4355

Eurocontrol: SAAM Reference Manual 4.2.0 Beta, Version 21-12-2012, edited by: Eurocontrol, p. 434, 2012. 4351

Eurocontrol: User guide AEM-kernel, Internal Document V2.26, T07/22317TC/C1107/05, Eurocontrol, 2013. 4351

Fichter, C.: Climate impact of air traffic emissions in dependency of the emission location and altitude, Dissertation, DLR-Forschungsbericht, DLR-FB-2009-22, 2009. 4370, 4372, 4409

Forster, P. M. de F. and Shine, K. P.: Radiative forcing and temperature trends from stratospheric ozone changes, J. Geophys. Res., 102, 10841–10857, 1997. 4367

Forster, P., Ramaswamy, V., Artaxo, P., Berntsen, T., Betts, R., Fahey, D. W., Haywood, J, Lean, J., Lowe, D. C., Myhre, G., Nganga, J., Prinn, R., Raga, G., Schulz, M., and Van Dorland, R.: Changes in atmospheric constituents and in radiative forcing, edited by: Solomon, S., Qin, D., Manning, M., Marquis, M., Averyt, K., Tignor, M. M. B., LeRoy Miller Jr., H., and Chen, Z., Climate Change 2007: the Physical Science Basis. Contribution of Working Group I to the Fourth Assessment Report of the Intergovernmental Panel on Climate Change, Cambridge University Press, Cambridge, 2007. 4367

GMDD
6, 4345–4416, 2013

Frömming, C., Ponater, M., Burkhardt, U., Stenke, A., Pechtl, S., and Sausen, R.: Sensitivity of contrail coverage and contrail radiative forcing to selected key parameters, Atmos. Environ., 45, 1483–1490, 2011. 4379

Frömming, C., Ponater, M., Dahlmann, K., Grewe, V., Lee, D. S., and Sausen, R.: Aviation-induced radiative forcing and surface temperature change in dependency of the emission altitude, J. Geophys. Res., 117, D19104, doi:10.1029/2012JD018204, 2012. 4347, 4376

Fuglestvedt, J., Berntsen, T., Myhre, G., Rypdal, K., and Skeie, R.: Climate forcing from the transport sectors, P. Natl. Acad. Sci. USA, 105, 454–458, 2008. 4377

Fuglestvedt, J. S., Shine, K. P., Berntsen, T., Cook, J., Lee, D. S., Stenke, A., Skeie, R. B., Velders, G. J. M., and Waitz, I. A.: Transport impacts on atmosphere and climate: metrics, Atmos. Environ., 44, 4648–4677, doi:10.1016/j.atmosenv.2009.04.044, 2010. 4367, 4373, 4375, 4380, 4395, 4397

Gierens, K. and Spichtinger, P.: On the size distribution of ice-supersaturated regions in the upper troposphere and lowermost stratosphere, Ann. Geophys., 18, 499–504, doi:10.1007/s00585-000-0499-7, 2000. 4347

Grewe, V.: A generalized tagging method, Geosci. Mod. Dev., 6, 247–253, 2013. 4356

Grewe, V. and Dahlmann, K.: Evaluating Climate-Chemistry Response and Mitigation Options with AirClim, 591–608, edited by: Schumann, U., ISBN 978-3-642-30182-7, ISBN 978-3-642-30183-4 (eBook), doi:10.1007/978-3-642-30183-4, Springer, Heidelberg, New York, Dordrecht, London, 2012. 4374, 4382

Grewe, V. and Stenke, A.: AirClim: an efficient tool for climate evaluation of aircraft technology, Atmos. Chem. Phys., 8, 4621–4639, doi:10.5194/acp-8-4621-2008, 2008. 4347, 4374, 4377, 4380, 4382, 4395, 4411

Grewe, V., Dameris, M., Fichter, C., and Sausen, R.: Impact of aircraft NO_x emissions. Part 1: interactively coupled climate-chemistry simulations and sensitivities to climate-chemistry feedback, lightning and model resolution, Meteorol. Z. 3, 177–186, 2002. 4376, 4377

Grewe, V., Tsati, E., and Hoor, P.: On the attribution of contributions of atmospheric trace gases to emissions in atmospheric model applications, Geosci. Model Dev., 3, 487–499, doi:10.5194/gmd-3-487-2010, 2010. 4355, 4356, 4359

Grewe, V., Dahlmann, K., Matthes, S., and Steinbrecht, W.: Attributing ozone to NO_x emissions: implications for climate mitigation measures, Atmos. Environ., 59, 102–107, 2012a. 4349, 4355, 4356

GMDD
6, 4345–4416, 2013

Grewe, V., Moussiopoulos, N., Builtjes, P., Borrego, C., Isaksen, I. S. A., and Volz-Thomas, A.: The ACCENT-protocol: a framework for benchmarking and model evaluation, Geosci. Model Dev., 5, 611–618, 2012b. 4378

Hansen, J., Sato, M., and Ruedy, R.: Radiative forcing and climate response, J. Geophys. Res., 102, 6831–6864, 1997. 4367, 4368, 4372

Heymsfield, A. J. and Donner, L. J.: A scheme for parameterizing ice cloud water content in general circulation models, J. Atmos. Sci., 47, 1865–1877, 1990. 4366

Heymsfield, A., Baumgardner, D., DeMott, P., Forster, P., Gierens, K., and Kärcher, B.: Contrail microphysics, B. Am. Meteorol. Soc., 91, 465–472, doi:10.1175/2009BAMS2839.1, 2010. 4378

Holmes, C. D., Tang, Q., and Prather, M. J.: Uncertainties in climate assessment for the case of aviation NO, P. Natl. Acad. Sci. USA, 108, 10997–11002, doi:10.1073/pnas.1101458108, 2011. 4377

IPCC, Climate Change 2007 – The physical science basis. Contribution of Working Group I to the Fourth Assessment Report of the Intergovernmental Panel on Climate Change Contributions of working group I, edited by: Solomon, S., Qin, D., Manning, M., Chen, Z., Marquis, M., Averyt, K. B., Tignor, M., and Miller, H. L., Cambridge University Press, Cambridge, UK, New York, NY, USA, 2007. 4347

Irvine, E. A., Hoskins, B. J., and Shine, K. P.: The dependence of contrail formation on the weather pattern and altitude in the North Atlantic, Geophys. Res. Lett., 39, L12802, doi:10.1029/2012GL051909, 2012. 4347

Irvine, E. A., Hoskins, B. J., Shine, K. P., Lunnon, R. W., and Frömming C.: Characterizing north Atlantic weather patterns for climate-optimal routing, Meteorol. Appl., 20, 80–93, doi:10.1002/met.1291, 2013. 4348, 4376

Iwabuchi, H., Yang, P., Liou, K. N., and Minnis, P.: Physical and optical properties of persistent contrails: climatology and interpretation, J. Geophys. Res., 117, D06215, doi:10.1029/2011JD017020, 2012. 4379

Jöckel, P., Tost, H., Pozzer, A., Brühl, C., Buchholz, J., Ganzeveld, L., Hoor, P., Kerkweg, A., Lawrence, M. G., Sander, R., Steil, B., Stiller, G., Tanarhte, M., Taraborrelli, D., van Aardenne, J., and Lelieveld, J.: The atmospheric chemistry general circulation model ECHAM5/MESSy1: consistent simulation of ozone from the surface to the mesosphere, Atmos. Chem. Phys., 6, 5067–5104, doi:10.5194/acp-6-5067-2006, 2006. 4350

GMDD
6, 4345–4416, 2013

Jöckel, P., Kerkweg, A., Pozzer, A., Sander, R., Tost, H., Riede, H., Baumgaertner, A., Gromov, S., and Kern, B.: Development cycle 2 of the Modular Earth Submodel System (MESSy2), Geosci. Model Dev., 3, 717–752, doi:10.5194/gmd-3-717-2010, 2010. 4350, 4356

Kärcher, B., Burkhardt, U., Unterstrasser, S., and Minnis, P.: Factors controlling contrail cirrus optical depth, Atmos. Chem. Phys., 9, 6229–6254, doi:10.5194/acp-9-6229-2009, 2009. 4378, 4379

Kärcher, B., Burkhardt, U., Ponater, M., and Frömming, C.: Importance of representing optical depth variability for estimates of global line-shaped contrail radiative forcing, P. Natl. Acad. Sci. USA, 107, 19181–19184, doi:10.1073/pnas.1005555107, 2010. 4379

Köhler, M. O., Rädel, G., Dessens, O., Shine, K. P., Rogers, H. L., Wild, O., and Pyle, J. A.: Impact of perturbations to nitrogen oxide emissions from global aviation, J. Geophys. Res., 113, D11305, doi:10.1029/2007JD009140, 2008. 4347, 4382

Lee, D. S., Pitari, G., Grewe, V., Gierens, K., Penner, J. E., Petzold, A., Prather, M. J., Schumann, U., Bais, A., Berntsen, T., Iachetti, D., Lim, L. L., and Sausen, R.: Transport impacts on atmosphere and climate: aviation, Atmos. Environ., 44, 4678–4734, 2010. 4347, 4377, 4378

Mannstein, H., Spichtinger, P., and Gierens, K.: A note on how to avoid contrail cirrus, Transport. Res., 10, 421–426, 2005. 4348

Marquart, S.: Klimawirkung von Kondensstreifen: Untersuchungen mit einem globalen atmosphärischen Zirkulationsmodell, Dissertation, DLR-Forschungsbericht 2003-16, p. 161, ISSN 1434-8454, Cologne, Germany, 2003. 4367

Marquart, S., Ponater, M., Mager, F., and Sausen, R.: Future development of contrail cover, optical depth and radiative forcing: impacts of increasing air traffic and climate change, J. Climate, 16, 2890–2904, 2003. 4378

Matthes, S.: Climate-optimised flight planning – REACT4C in Innovation for a Sustainable Aviation in a Global Environment, Proceedings of the Sixth European Aeronautics Days 2011, IOS Press & European Union, ISBN 978-92-79-22968-8, 2012. 4348

Matthes, S., Schumann, U., Grewe, V., Frömming, C., Dahlmann, K., Koch, A., and Mannstein, H.: Climate Optimized Air Transport, edited by: Schumann, U., ISBN 978-3-642-30182-7, ISBN 978-3-642-30183-4 (eBook), doi:10.1007/978-3-642-30183-4, Springer, Heidelberg, New York, Dordrecht, London, 727–746, 2012. 4348

GMDD
6, 4345–4416, 2013

Minnis, P., Young, D. F., Nguyen, L., Garber, D. P., Smith Jr., W. L., and Palikonda, R.: Transformation of contrails into cirrus durring SUCCESS, Geophys. Res. Lett., 25, 1157–1160, 1998. 4347

Myhre, G., Kvalevåg, M. M., Rädel, G., Cook, J., Shine, K. P., Karcher, F., Markowicz, K., Kardas, A., Wolkenberg, P., Balkanski, Y., Ponater, M., Forster, P. M., Rap, A., and Rodriguez de Leon, R.: Intercomparison of radiative forcing of stratospheric water vapour and contrails, Met. Z., 18, 585–596, 2009. 4379, 4414, 4415

Ponater, M., Marquart, S., and Sausen, R.: Contrails in a comprehensive global climate model: parameterization and radiative forcing results, J. Geophys. Res., 107, 941–960, 2002. 4365, 4366

Rädel, G. and Shine, K. P.: Radiative forcing by persistent contrails and its dependence on cruise altitudes, J. Geophys. Res., 113, D07105, doi:10.1029/2007JD009117, 2008. 4382

Reithmeier, C. and Sausen, R.: ATTILA – atmospheric tracer transport in a Lagrangian model, Tellus B, 54, 278–299, 2002. 4349

Roeckner, E., Brokopf, R., Esch, M., Giorgetta, M., Hagemann, S., Kornblueh, L., Manzini, E., Schlese, U., and Schulzweida, U.: Sensitivity of simulated climate to horizontal and vertical resolution in the ECHAM5 atmosphere model, J. Climate, 19, 3771–3791, 2006. 4350

Sander, R., Baumgaertner, A., Gromov, S., Harder, H., Jöckel, P., Kerkweg, A., Kubistin, D., Regelin, E., Riede, H., Sandu, A., Taraborrelli, D., Tost, H., and Xie, Z.-Q.: The atmospheric chemistry box model CAABA/MECCA-3.0, Geosci. Model Dev., 4, 373–380, doi:10.5194/gmd-4-373-2011, 2011. 4350

Sausen, R., Nodorp, D., and Land, C.: Towards an optimal flight routing with respect to minimal environmental impact, in: Impact of Emissions from Aircraft and Spacecraft upon the Atmosphere, edited by: Schumann, U. and Wurzel, D., Procedings of an International Science Colloquium, Köln (Cologne), Germany, 18–20 April, ISSN 0939-298X, 473–478, 1994. 4348

Schröder, F., Kärcher, B., Duroure, C., Ström, J., Petzold, A., Gayet, J.-F., Strauss, B., Wendling, P., and Borrmann, S.: On the transition of contrails into cirrus clouds, J. Atmos. Sci., 57, 464–480, doi:10.1175/1520-0469(2000)057<0464:OTTOCI>2.0.CO;2, 2000. 4378

Schumann, U.: On conditions for contrail formation from aircraft exhausts, Meteorol. Z., 5, 4–23, 1996. 4347, 4363

Schumann, U.: Influence of propulsion efficiency on contrail formation, Aerosp. Sci. Technol., 4, 391–401, 2000. 4392

GMDD
6, 4345–4416, 2013

Schumann, U.: A contrail cirrus prediction model, Geosci. Model Dev., 5, 543–580, doi:10.5194/gmd-5-543-2012, 2012. 4378
Schumann, U., Graf, K., and Mannstein, H.: Potential to reduce the climate impact of aviation by flight level changes. 3rd AIAA Atmospheric and Space Environments Conference AIAA paper 2011-3376, 1–22, 2011. 4348
Shine, K. P. Derwent, R. G., Wuebbles, D. J., and Morcrette, J.-J.: Radiative forcing of climate, in: Climate Change: The IPCC Scientific Assessment (1990), Report prepared for Intergovernmental Panel on Climate Change by Working Group I, edited by: Houghton, J. T., Jenkins, G. J., and Ephraums, J. J., Cambridge University Press, Cambridge, Great Britain, New York, NY, USA and Melbourne, Australia, 410 pp., 41–68, 1990. 4374, 4395
Spichtinger, P., Gierens, K., Leiterer, U., and Dier, H.: Ice supersaturation in the tropopause region over Lindenberg, Germany, Meteorol. Z., 12, 143–156, 2003. 4347
Sridhar, B., Chen, N., and Ng, H.: Energy Efficient Strategies for Reducing the Environmental Impact of Aviation, paper 212, 10th ATM-seminar, Chicago, USA, pp. 10, available at: www.atmseminar.org (last access: August 2013), 2012. 4348
Stevenson, D. S., Doherty, R. M., Sanderson, M. G., Collins, W. J., Johnson, C. E., and Derwent, R. G.: Radiative forcing from aircraft NO_x emissions: mechanisms and seasonal dependence, J. Geophys. Res., 109, D17307, doi:10.1029/2004JD004759, 2004. 4376, 4412
Stevenson, D. S., Dentener, F. J., Schultz, M. G., Ellingsen, K., van Noije, T. P. C., Wild, O., Zeng, G., Amann, M., Atherton, C. S., Bell, N., Bergmann, D. J., Bey, I., Butler, T., Cofala, J., Collins, W. J., Derwent, R. G., Doherty, R. M., Drevet, J., Eskes, H. J., Fiore, A. M., Gauss, M., Hauglustaine, D. A., Horowitz, L. W., Isaksen, I. S. A., Krol, M. C., Lamarque, J.-F., Lawrence, M. G., Montanaro, V., Müller, J.-F., Pitari, G., Prather, M. J., Pyle, J. A., Rast, S., Rodriguez, J. M., Sanderson, M. G., Savage, N. H., Shindell, D. T., Strahan, S. E., Sudo, K., and Szopa, S.: Multimodel ensemble simulations of present-day and near-future tropospheric ozone, J. Geophys. Res., 111, D08301, doi:10.1029/2005JD006338, 2006. 4382
Stuber, N.: Ursachen der Variabilität des Klimasensitivitätsparameters für räumlich inhomogene Ozonstörungen, Dissertation, DLR-Forschungsbericht 2003-03, 2003. 4372, 4409
Stuber, N., Sausen, R., and Ponater, M.: Stratosphere adjusted radiative forcing calculations in a comprehensive climate model, Theor. Appl. Climatol., 68, 125–135, 2001. 4367, 4372
Voigt, C., Schumann, U., Jessberger, P., Jurkat, T., Petzold, A., Gayet, J.-F., Krämer, M., Thornberry, T., and Fahey, D. W.: Extinction and optical depth of contrails, Geophys. Res. Lett., 38, L11806, doi:10.1029/2011GL047189, 2011. 4378, 4379

GMDD
6, 4345–4416, 2013

Wilcox, L. J., Shine, K. P., and Hoskins, B. J.: Radiative forcing due to aviation water vapour emissions, Atmos. Environ., 63, 1–13, doi:10.1016/j.atmosenv.2012.08.072, 2012. 4377

GMDD
6, 4345–4416, 2013

Table 1. Definition of the time-region grid.

Dimension	Number	Unit	Values
Longitude	6	°W	75, 60, 45, 30, 15, 0
Latitude	7	°N	30, 35, 40, 45, 50, 60, 80
Pressure	4	hPa	400, 300, 250, 200
Time	3	UTC	6, 12, 18

GMDD
6, 4345–4416, 2013

Table 2. Emissions and aircraft/fuel parameters.

Parameter	Units	Value	Comment
NO_x emission	kg(NO)	5×10^5	Equals 2.33×10^5 kg(N) and takes place during a 15 min time step
H_2O emission	kg	1.25×10^7	Takes place during a 15 min time step
Overall propulsion efficiency	–	0.31	see Schumann (2000)
H_2O emission index	kg(H_2O) (kg(fuel))$^{-1}$	1.25	Schumann (2000)
Kerosene combustion heat	J kg^{-1}	43.2×10^6	Schumann (2000)

GMDD
6, 4345–4416, 2013

Table 3. Parameters of the contrail parameterisation.

Parameter	Value	Unit	Description
W_0	200	m	Initial contrail width
A	variable	m^2	Grid box area
D	$\sqrt{A}$	m	Flown distance in the grid box
L	$D\, b_{co}$	m	Initial contrail length
Δt	900	s	Timestep (15 min)
H	200	m	Initial contrail thickness
c	0.72	–	Scaling factor for contrail spreading
m_{thres}	10^{-10}	$kg\,kg^{-1}$	Water vapour mixing ratio threshold for contrail coverage

GMDD
6, 4345–4416, 2013

Table 4. Parameters of the CO_2 parameterisation.

Parameter	Value	Unit	Description
EI_{CO_2}	3.16	$kg(CO_2)\,(kg(fuel))^{-1}$	CO_2 emission index
a_i	0.217; 0.259; 0.388; 0.186	–	Weighting factors
α_i	∞; 172.9; 18.51; 1.186	yr	Lifetime

GMDD
6, 4345–4416, 2013

Table 5. Overview on radiative forcing calculation for various species. "A" and "I" mean adjusted and instantaneous radiative forcing in the column "RF-type".

Species	Concentration	RF-type	radiative forcing
CO_2	Response-Formula (Eq. 47)[1]	A	$1.82 \times 10^{-12}\,\mathrm{mW\,m^{-2}\,kg(CO_2)^{-1}}$)[1]
O_3	EMAC (Eq. 10)	A	EMAC
CH_4	EMAC (Eq. 30)	A	IPCC-formula[2]
PMO	–	A	$-0.29\ \mathrm{RF(PMO)/RF(CH_4)}$[3]
H_2O	EMAC	A	$4.38 \times 10^{-13}\,\mathrm{W\,m^{-2}\,kg(H_2O)^{-1}}$)[4]
Contrails	EMAC	I	EMAC

[1] Fuglestvedt et al. (2010).
[2] Shine et al. (1990).
[3] Dahlmann (2012).
[4] this work based on data from Grewe and Stenke (2008).

GMDD
6, 4345–4416, 2013

Table 6. Overview on objectives and implied emission scenarios and climate metrics or indicators. ATR is the average temperature response; AGTP is the absolute global temperature potential; AGWP is the absolute global warming potential; the number after the metrics give the time horizon in years.

Q1: What is the **shortterm** climate impact of the REACT4C re-routing strategy?		Q2: What is the **longterm** climate impact of the REACT4C re-routing strategy?		Q3: What is the medium climate impact of a **today's** REACT4C re-routing decision?	
Emission	Metric	Emission	Metric	Emission	Metric
Future air traffic scenario	ATR20	Future air traffic scenario	ATR100	Pulse emission	ATR50
Sustained emissions	ATR20	Sustained emissions	ATR100	Pulse emission	AGTP50
Sustained emissions	AGTP20	Sustained emissions	AGTP100		
Pulse emission	AGWP20	Pulse emission	AGWP100		
Role of atmospheric processes					
Short-term atmospheric effects are important Focus on contrails and ozone		Short- and long-term atmospheric effects are important Focus on all species		Long-term atmospheric effects are important Focus on carbon dioxide	

GMDD
6, 4345–4416, 2013

Table 7. Comparison of simulated GWP20, GWP100, and GTP50 values for ozone (short-lived only) and methane for emissions of NO_x in the domain indicated in Table 1 with results from three different studies published in Fuglestvedt et al. (2010), abbreviated with F10.

	GWP20		GWP100		GTP50	
	Ozone	Methane	Ozone	Methane	Ozone	Methane
F10	670/1100/1800	−460/ − 490/ − 850	190/300/510	−160/ − 170/ − 320	33/52/88	−75/ − 85/ − 190
200 hPa	1050	−880	300	−310	51	−150
250 hPa	760	−1060	220	−370	37	−180
300 hPa	890	−1110	250	−390	43	−190
400 hPa	860	−1060	240	−370	42	−180

GMDD
6, 4345–4416, 2013

Table A1. Abbreviations.

AEM	Advanced Emission Model
ATTILA	Atmospheric Tracer Transport in a Lagrangian Model
BADA	Base of Aircraft Data
CCF	Climate Cost Function
GFED	Global Fire Emissions Database
ECHAM	ECMWF general circulation model - Hamburg version
ECMWF	European Centre for Medium-Range Weather Forecasts
EMAC	ECHAM/MESSy Atmospheric Chemistry
PMO	Primary Mode Ozone
RAD	Route Availability Document
REACT4C	React for climate
RETRO	REanalysis of the TROpospheric chemical composition over the past 40 yr
RF	Radiative Forcing
SAAM	System for traffic Assignment and Analysis at a Macroscopic level

GMDD
6, 4345–4416, 2013

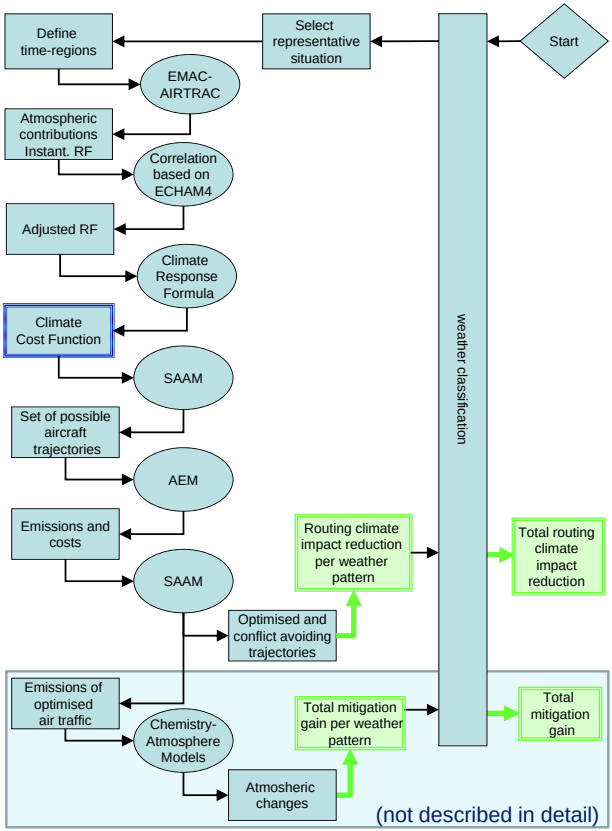

Fig. 1. Illustration of the model chain. Models are given in ovals. Data and definitions are given in rectangles. Climate cost functions are highlighted (dark blue) as well as major results (green). The shaded area indicates a possible extension of the modelling chain, which is not covered here.

GMDD
6, 4345–4416, 2013

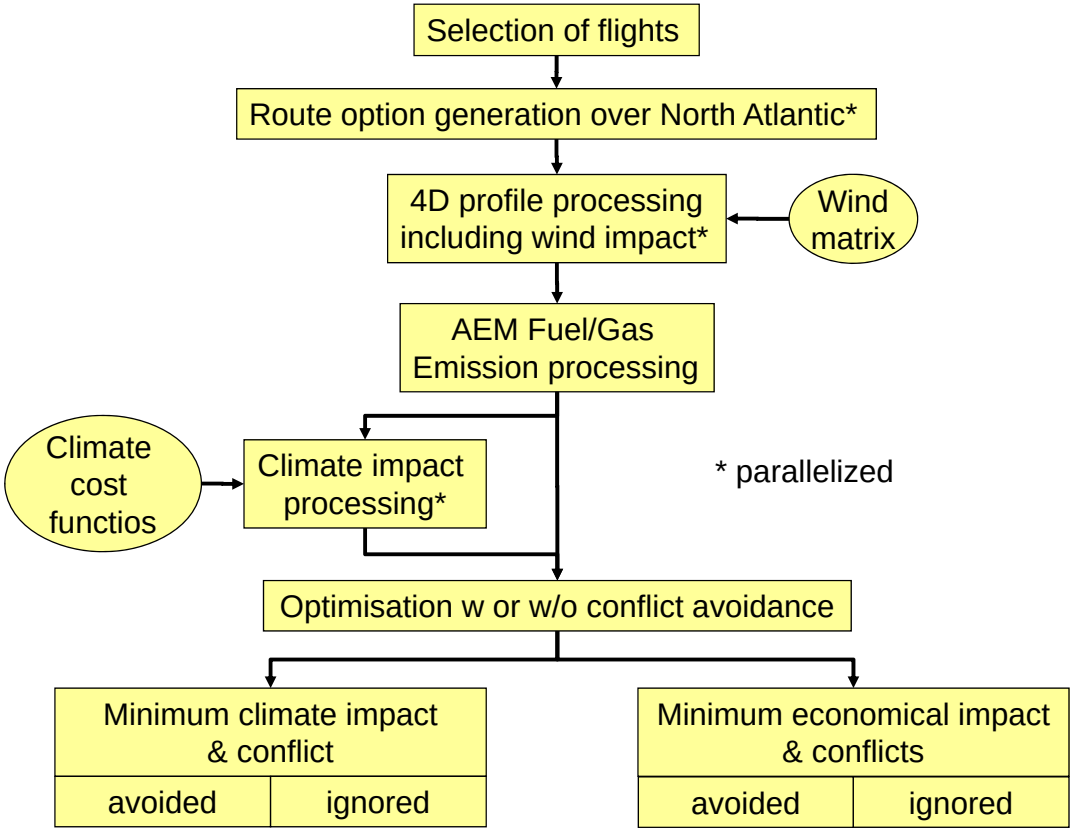

Fig. 2. Illustration of the SAAM and AEM model interaction.

GMDD
6, 4345–4416, 2013

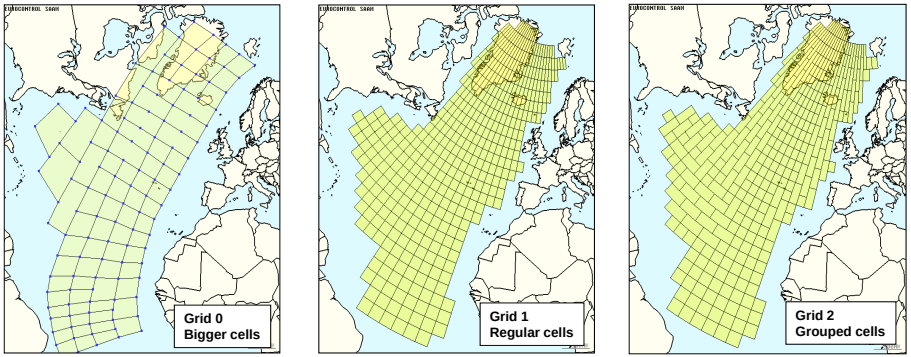

Fig. 3. Different grid resolutions for route generation.

GMDD
6, 4345–4416, 2013

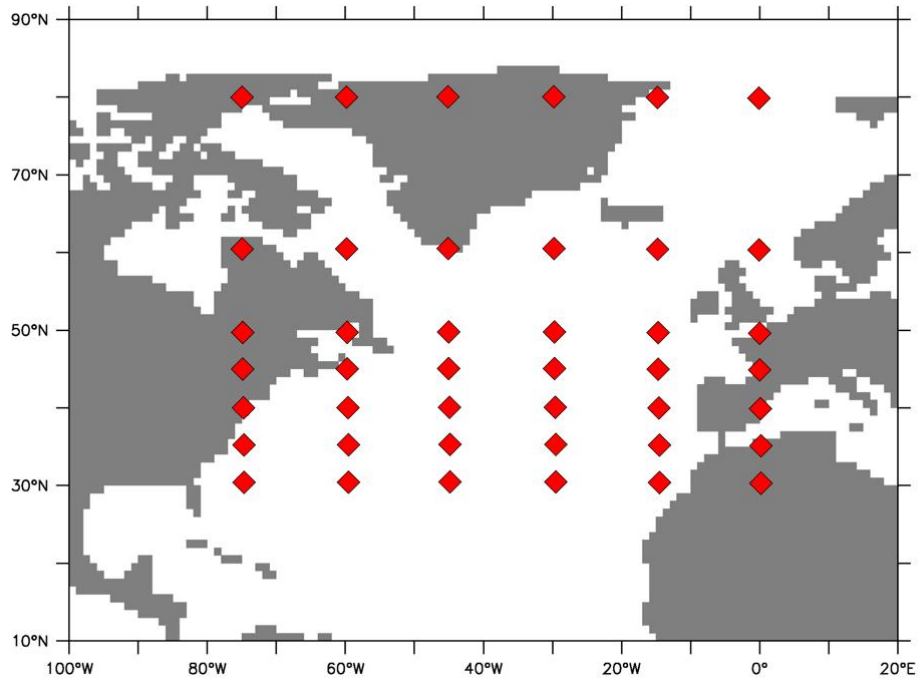

Fig. 4. Time-region properties in the submodel AIRTRAC.

GMDD
6, 4345–4416, 2013

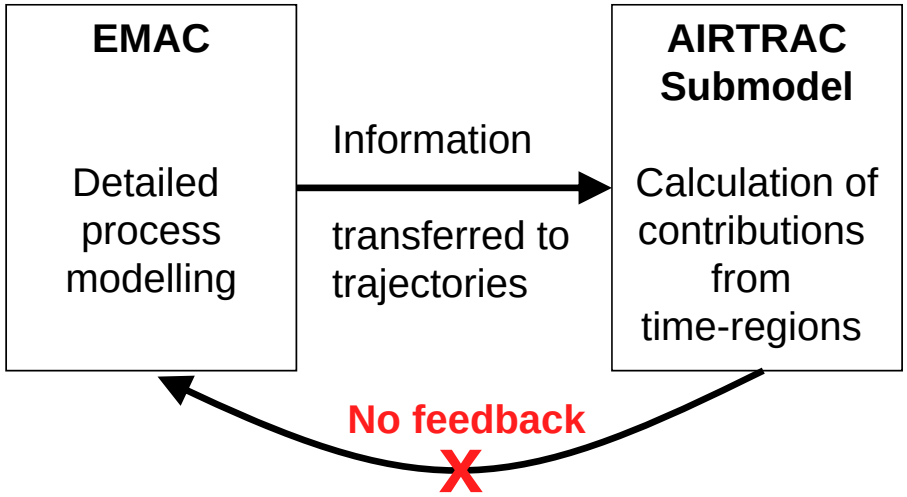

Fig. 5. Coupling of AIRTRAC with EMAC.

GMDD
6, 4345–4416, 2013

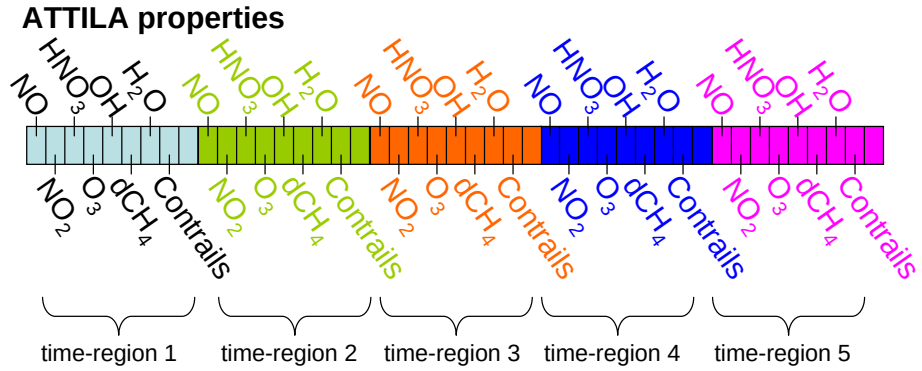

Fig. 6. Latitude–longitude grid of the climate cost function.

GMDD
6, 4345–4416, 2013

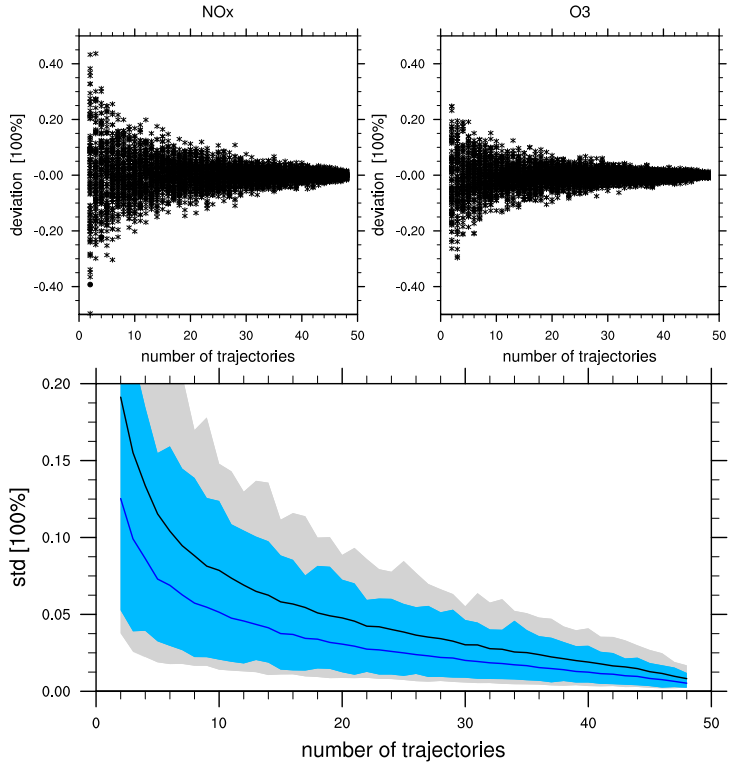

Fig. 7. Top: deviations of possible results of the monthly mean January NO_x mixing ratio (left) and ozone mixing ratio (right) for emissions at 200 hPa and 50° N, 45° W as a function of the number of trajectories simulated. The deviation is relative to the result using 50 trajectories. Bottom: the standard deviations of the results for NO_x and ozone as shown as a function of the number of trajectories used for 24 different emission points (shading: gray for NO_x and blue for ozone) and the mean of the standard deviation over the 24 points (upper black line for NO_x, lower dark blue line for ozone).

GMDD
6, 4345–4416, 2013

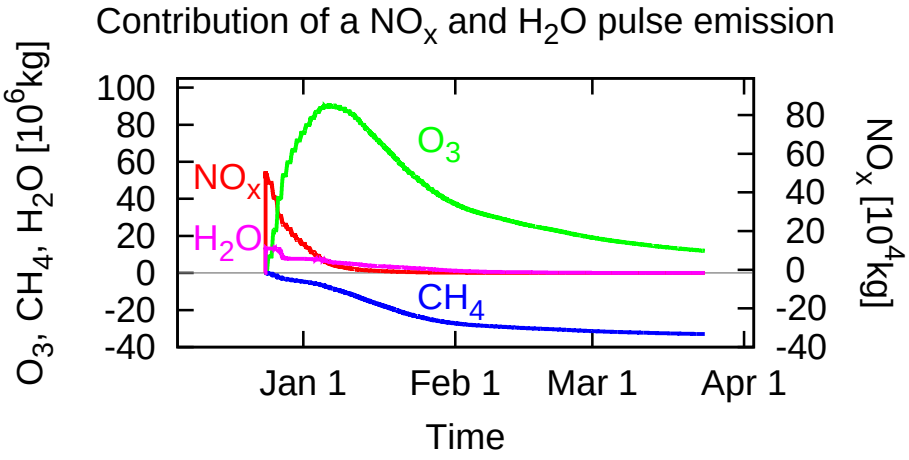

Fig. 8. Contributions from NO_x and H_2O emissions in a time-region (here: 75° W, 30° N, 200 hPa, 06:00 UTC) to NO_x (red), ozone (green), methane (blue), and water vapour (magenta) global atmospheric masses [kg].

GMDD
6, 4345–4416, 2013

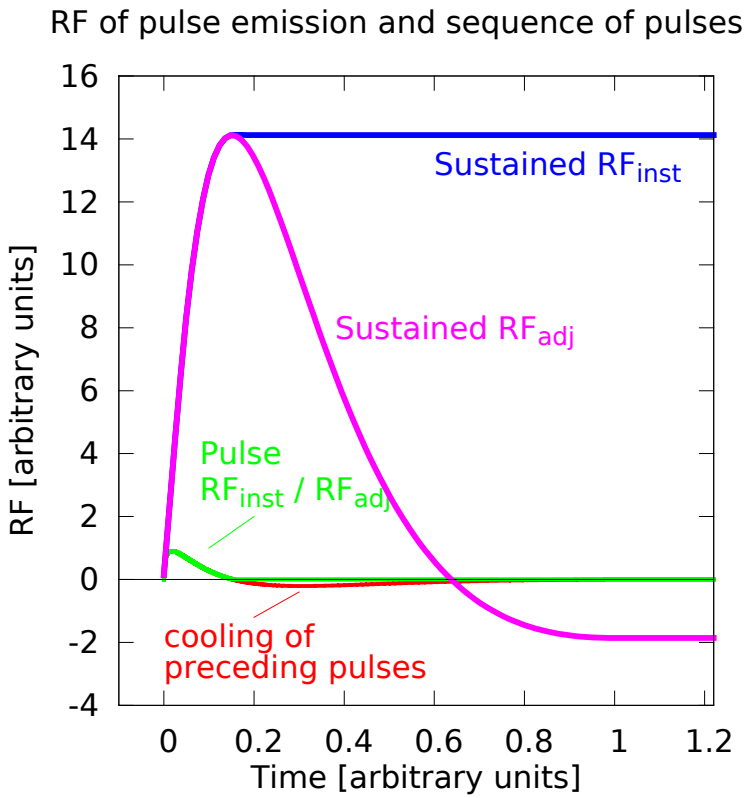

Fig. 9. Schematic view of the radiative forcing due to ozone as a result of a pulse emission of NO_x compared to a sequence of pulse emissions (= sustained emissions). Instantaneous and adjusted RF of a short pulse emission are identical (green). Instantaneous RF of a sequence of pulse emissions (magenta) is calculated as the sum of the instantaneous RF of pulse emissions. Adjusted RF of a sequence of pulse emissions (blue) is calculated similarly, i.e. as the sum of the RF of a sequence of pulse emissions, where the cooling effect of preceding pulses is parameterised (red).

GMDD
6, 4345–4416, 2013

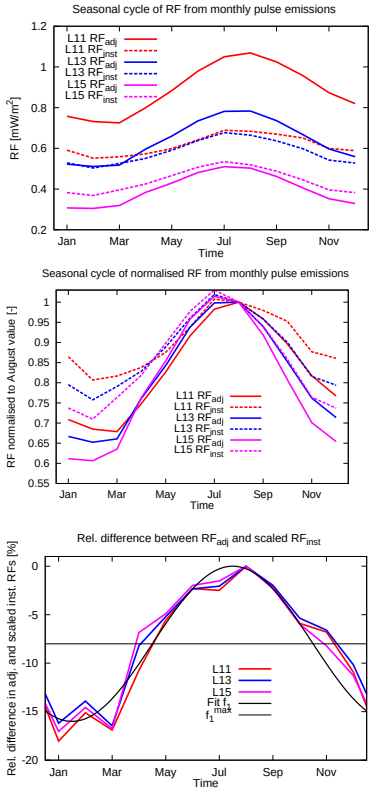

Fig. 10. Annual cycle of the radiative forcing due to ozone change of a pulse emission of NO_x. The NO_x emission, which produces the monthly change pattern is located at 130 hPa (L11, red), 160 hPa (L13, blue), and 200 hPa (L15, magenta). Dashed lines refer to instantaneous RF and solid to adjusted RF. **(a)** Seasonal cycle of RF. **(b)** as **(a)**, but normalised to the individual August value, **(c)** Relative difference [%] of the adjusted RF and the scaled instantaneous RF. The scaling factor is the quotient of the respective August values. The black line shows a sine fit f_1, see Eq. (50).

GMDD
6, 4345–4416, 2013

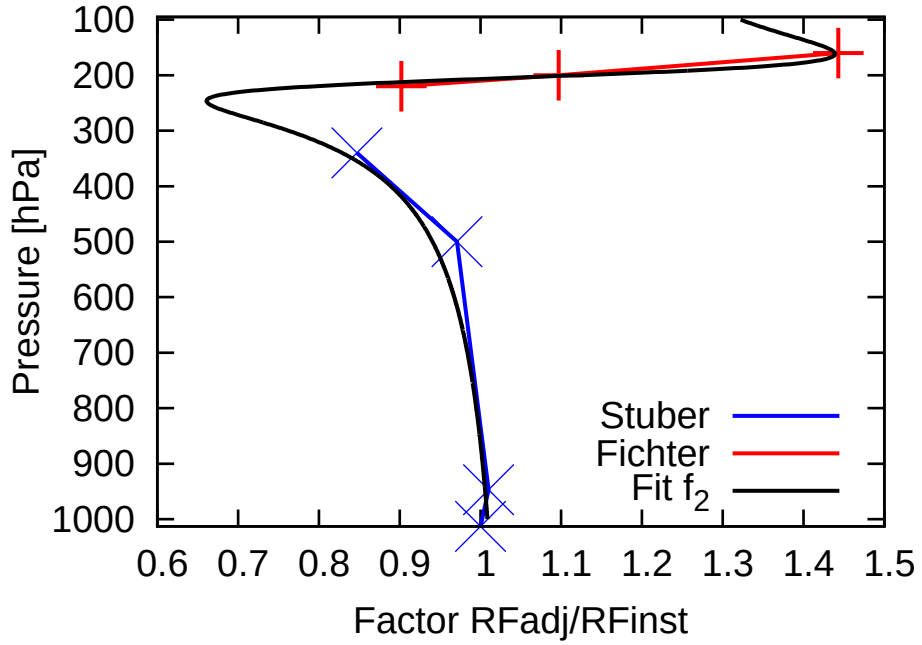

Fig. 11. Height dependence of the relation between instantaneous and adjusted RF for annual mean RF values for changes in ozone. Data are taken from Stuber (2003); Fichter (2009). Ozone changes are mainly located on the Northern Hemisphere (see also Supplement).

GMDD
6, 4345–4416, 2013

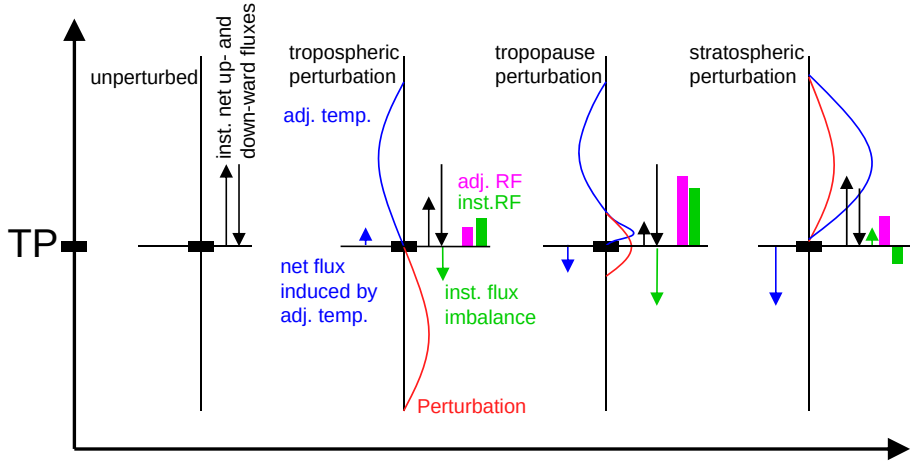

Fig. 12. Schematic of the relation between instantaneous (green bar) and adjusted RF (magenta bar) for ozone changes for 4 situations: unperturbed, tropospheric perturbation, tropopause perturbation, stratospheric perturbation (from left to right). The perturbation pattern is given as a red line, the instantaneous upward and downward net flux changes are given as black arrows. Net flux means the sum of longwave and shortwave fluxes. The adjusted stratospheric temperatures are shown as a blue line, the resulting net flux changes as blue arrows. For details characterising the different cases, see text.

GMDD
6, 4345–4416, 2013

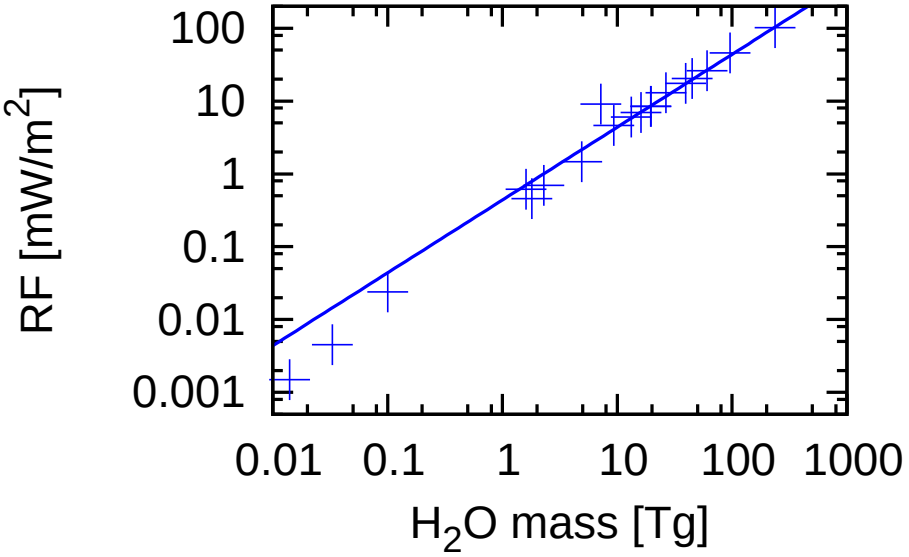

Fig. 13. Relation between change in atmospheric water vapour [Tg] and adjusted radiative forcing [mW m^{-2}]. Data are from Grewe and Stenke (2008). The line represents a fit with with RF = 4.38×10^{-13} W m^{-2} kg^{-1}.

GMDD
6, 4345–4416, 2013

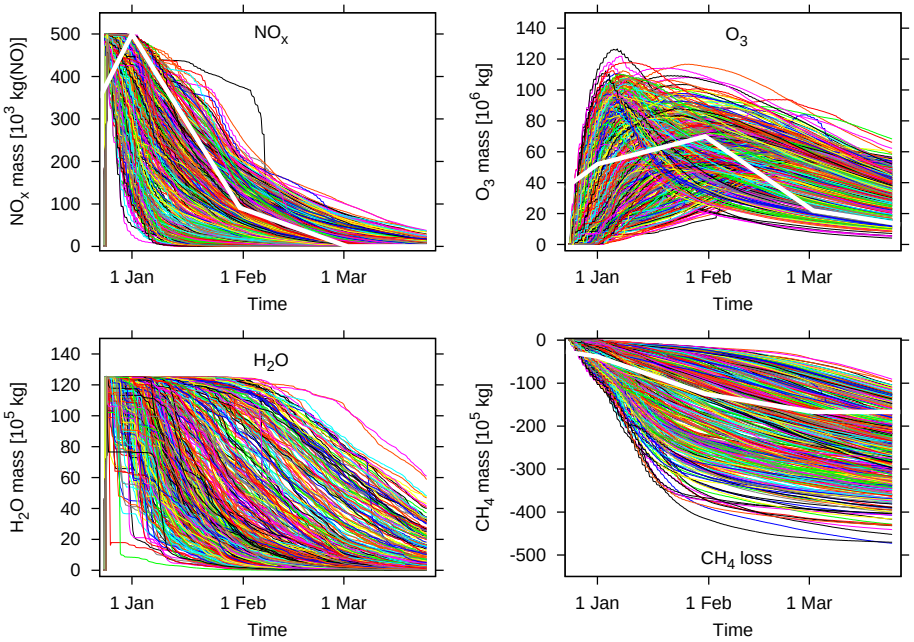

Fig. 14. Temporal evolution of global mean masses of NO_x [10^3 kg(NO)], O_3 [10^6 kg], H_2O [10^5 kg], CH_4 [10^5 kg]. For every time-region (= grid point of the climate cost function; see Table 1), 50 trajectories are started and the temporal evolution of the global mean over these 50 trajectories is presented. I.e. each colored line (in total 504) represents the temporal evolution of species caused by an emissions at the respective time-region. The white lines indicate results from Stevenson et al. (2004) scaled by the factor 6.94×10^{-3} to derive the same initial NO_x perturbation. Note that values by Stevenson et al. (2004) are monthly means.

GMDD
6, 4345–4416, 2013

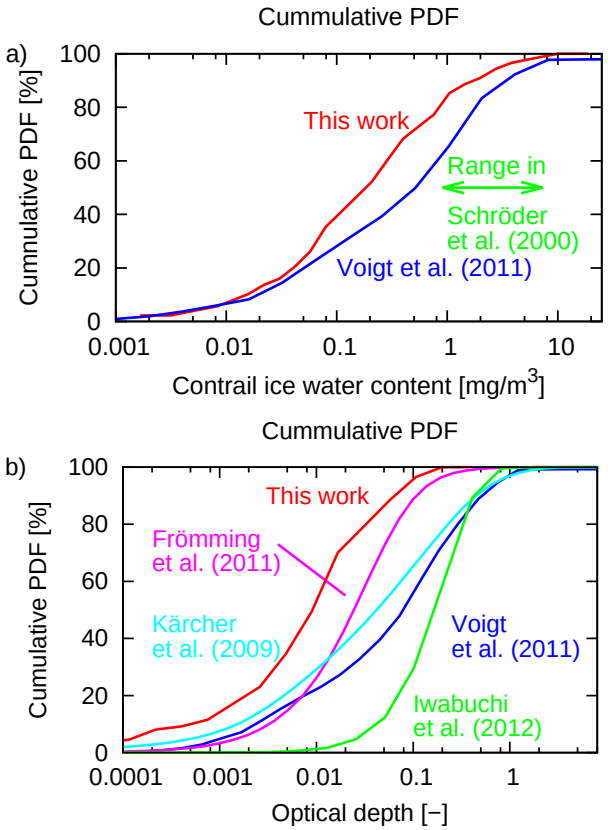

Fig. 15. Intercomparison of observed and simulated distributions of contrail properties. Estimated cummulative probability density functions of contrail ice water content [mg m^{-3}] **(a)** and **(b)** optical depth.

GMDD
6, 4345–4416, 2013

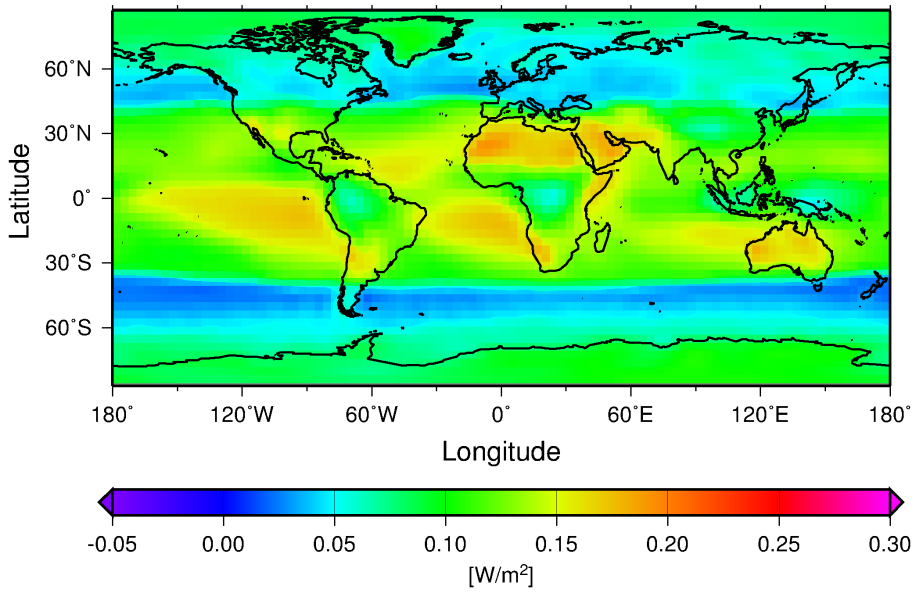

Fig. 16. Geographical distribution of the annual mean all sky net radiative forcing at the top of the atmosphere for a homogeneous 1 % contrail cover simulated with EMAC, according to the benchmark test by Myhre et al. (2009).

GMDD
6, 4345–4416, 2013

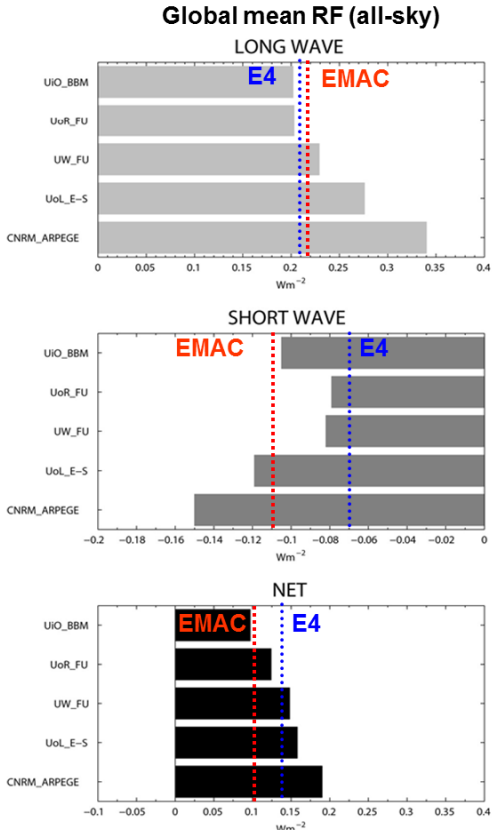

Fig. 17. Global means for the longwave (top), shortwave (mid) and net RF (bottom) for the contrail RF benchmark test (see text for details). Figure is adapted from Myhre et al. (2009).

GMDD
6, 4345–4416, 2013

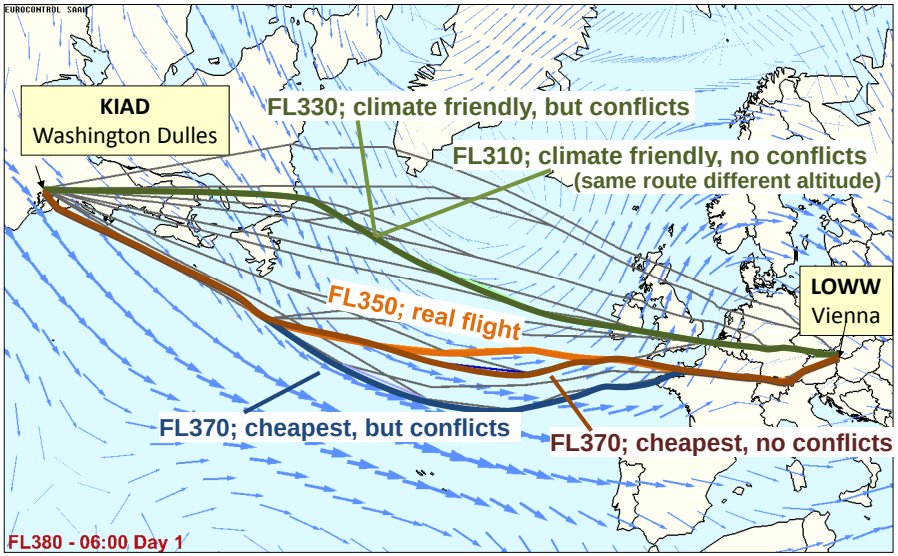

Fig. 18. Example for climate optimised flights, The optimisation was performed with respect to question Q2 (short-term climate impacts, AGWP20, see Table 6) for one particular winter weather pattern (strong zonally jet). The selected city pair connection is Washington to Vienna. The real flight at that day is shown in light brown. The economic optimal flights without conflict avoidance is given in blue and the conflict avoidance is given in dark brown. The climate optimal flights are shown in green. In this case the trajectories with and without conflict avoidance differ only in cruise altitude. Arrows indicate the wind field at flight level 380.

GMDD
6, 4345–4416, 2013